JEM Journal of Experimental Medicine

ARTICLE

Epitope convergence of broadly HIV-1 neutralizing IgA and IgG antibody lineages in a viremic controller

Valérie Lorin[1,2,3*], Ignacio Fernández[4,5*], Guillemette Masse-Ranson[6,7], Mélanie Bouvin-Pley[8], Luis M. Molinos-Albert[1,2], Cyril Planchais[1,2], Thierry Hieu[1,2], Gérard Péhau-Arnaudet[9], Dominik Hrebík[10], Giulia Girelli-Zubani[6,7], Oriane Fiquet[6,7], Florence Guivel-Benhassine[5,11], Rogier W. Sanders[12,13], Bruce D. Walker[14,15], Olivier Schwartz[5,11], Johannes F. Scheid[16], Jordan D. Dimitrov[17], Pavel Plevka[10], Martine Braibant[8], Michael S. Seaman[18], François Bontems[4,19], James P. Di Santo[6,7], Félix A. Rey[4,5], and Hugo Mouquet[1,2]

Decrypting the B cell ontogeny of HIV-1 broadly neutralizing antibodies (bNAbs) is paramount for vaccine design. Here, we characterized IgA and IgG bNAbs of three distinct B cell lineages in a viremic controller, two of which comprised only IgG$^+$ or IgA$^+$ blood memory B cells; the third combined both IgG and IgA clonal variants. 7-269 bNAb in the IgA-only lineage displayed the highest neutralizing capacity despite limited somatic mutation, and delayed viral rebound in humanized mice. bNAbs in all three lineages targeted the N332 glycan supersite. The 2.8-Å resolution cryo-EM structure of 7-269-BG505 SOSIP.664 complex showed a similar pose as 2G12, on an epitope mainly composed of sugar residues comprising the N332 and N295 glycans. Binding and cryo-EM structural analyses showed that antibodies from the two other lineages interact mostly with glycans N332 and N386. Hence, multiple B cell lineages of IgG and IgA bNAbs focused on a unique HIV-1 site of vulnerability can codevelop in HIV-1 viremic controllers.

Introduction

HIV-1 broadly neutralizing antibodies (bNAbs) develop in rare infected humans, termed Elite neutralizers, as a result of a complex co-evolution process with diversifying viruses (Doria-Rose and Landais, 2019; Victora and Mouquet, 2018). Over the past decade, hundreds of bNAbs have been isolated, some of which can protect nonhuman primates from infection (Nishimura and Martin, 2017) and decrease viremia in infected humans (Caskey et al., 2019). Apart from neutralization, Fc-dependent effector functions of bNAbs contribute to eliminating infected cells in vivo (Bournazos et al., 2014; Bruel et al., 2016; Lu et al., 2016) and boosting autologous cellular and humoral immune responses in recipients (Niessl et al., 2020; Schoofs et al., 2019). Hence, bNAbs hold great promise for HIV-1 treatment and prevention by vaccination or passive immunoprophylaxis (Klein et al., 2013). Yet, to elicit bNAbs by vaccination remains a challenge (Stephenson et al., 2020; Victora and Mouquet, 2018). bNAbs target a handful of vulnerability sites on the HIV-1 surface envelope glycoprotein 160 (gp160): the CD4 binding site (CD4bs), the *N*-glycan-associated V3 loop and V1/V2 loops, the gp120 "silent face," the *N*-glycan-associated gp120/gp41 bridging region, the membrane proximal external region, and the fusion peptide on gp41 (McCoy, 2018). Epitopes on the *N*-glycan–associated V3 loop, referred as the N332 supersite or the high-mannose patch, are of particular interest for vaccine design since they are frequently targeted by various classes of bNAbs (Daniels and Saunders, 2019), which may not require prolonged maturation pathways to be generated (MacLeod et al., 2016). Despite strain variations, the cluster of glycans centered on N332/N334 generally includes the potential *N*-glycosylation sites (PNGSs) at position N295,

[1]Laboratory of Humoral Immunology, Department of Immunology, Institut Pasteur, Paris, France; [2]Institut national de la santé et de la recherche médicale U1222, Paris, France; [3]Université de Paris, Sorbonne Paris Cité, Paris, France; [4]Structural Virology Unit, Department of Virology, Institut Pasteur, Paris, France; [5]Centre national de la recherche scientifique URA3015, Paris, France; [6]Innate Immunity Unit, Department of Immunology, Institut Pasteur, Paris, France; [7]Institut national de la santé et de la recherche médicale U1223, Paris, France; [8]Université de Tours, Institut national de la santé et de la recherche médicale U1259, Tours, France; [9]Imagopole, Plate-Forme de Microscopie Ultrastructurale and UMR 3528, Institut Pasteur, Paris, France; [10]Central European Institute of Technology, Masaryk University, Brno, Czech Republic; [11]Virus and Immunity Unit, Department of Virology, Institut Pasteur, Paris, France; [12]Department of Medical Microbiology, Amsterdam Infection and Immunity Institute, Amsterdam University Medical Centers, University of Amsterdam, Amsterdam, The Netherlands; [13]Department of Microbiology and Immunology, Weill Medical College of Cornell University, New York, NY; [14]Ragon Institute of Massachusetts General Hospital, MIT, and Harvard, Cambridge, MA; [15]Partners AIDS Research Center, Massachusetts General Hospital and Harvard Medical School, Charlestown, MA; [16]Laboratory of Molecular Immunology, The Rockefeller University, New York, NY; [17]Centre de Recherche des Cordeliers, Institut national de la santé et de la recherche médicale, Sorbonne Université, Université de Paris, Paris, France; [18]Beth Israel Deaconess Medical Center, Boston, MA; [19]Institut de Chimie des Substances Naturelles, Centre national de la recherche scientifique, Université Paris Saclay, Gif-sur-Yvette, France.

*V. Lorin and I. Fernández are co-first authors on this paper; Correspondence to Hugo Mouquet: hugo.mouquet@pasteur.fr; Félix A. Rey: felix.rey@pasteur.fr

N301, N386, and N392 (Behrens et al., 2016; Pritchard et al., 2015). The majority of N332-supersite bNAbs target distinct subepitopes comprising the N332 glycan, various neighboring glycans, and the ^{324}GDIR^{327} peptide at the base of the V3 loop (Daniels and Saunders, 2019). V3-glycan antibody lineages include PGT121-PGT124/10-1074, PGT125-PGT128, DH270.1, BF520.1, PCDN33, PGDM11-14, PGDM31, and BG8/BG18 (Bonsignori et al., 2017; Freund et al., 2017; Mouquet et al., 2012; Simonich et al., 2016; Sok et al., 2016; Walker et al., 2011). First-generation bNAb 2G12 (Trkola et al., 1996) and members of the PGT135-PGT137 family (Walker et al., 2011) recognized alternative epitopes within the N332-supersite (Daniels and Saunders, 2019).

All bNAbs identified belonged to the IgG class until recently, when genuine IgA bNAbs targeting the V3 loop crown (M4008_N1) and the V5-V2 loop corridor (M1214_N1) were described (Jia et al., 2020). However, the contribution of naturally induced and vaccine-induced anti-gp160 IgA antibodies is poorly understood and still debated (Lopez et al., 2018). IgAs have been proposed to negatively modulate Fc-effector functions of IgG antibodies in viremic subjects and RV144 vaccinees (Ruiz et al., 2016; Tomaras et al., 2013). Yet, nonneutralizing IgAs induced by RV144 vaccination may possess important antiviral properties for blocking mucosal transmission (Wills et al., 2018). IgA antibodies are indeed thought to play an important role at mucosal sites for reducing viral infection and spread (Lopez et al., 2018), despite potential decreased efficacy compared with IgGs (Astronomo et al., 2016; Cheeseman et al., 2017; Tay et al., 2016). Strikingly, HIV-1 elite controllers develop strong high-affinity IgA responses (Nabi et al., 2017), and cross-clade IgA-mediated seroneutralization has been found in long-term survivors (Planque et al., 2010). Whether HIV-1 controllers can produce IgA bNAbs with efficient antiviral functions in vivo remains unknown.

Here, we provide a detailed molecular and functional characterization of the IgA and IgG bNAbs expressed by three distinct B cell lineages developing in a viremic controller. We found that all bNAb lineages converge to target the high-mannose patch centered on the N332 glycan, with binding characteristics resembling 2G12. The most potent neutralizer isolated from the HIV-1 controller, 7-269 IgA bNAb, showed a neutralization breadth of 47% despite having undergone modest somatic mutation and displayed in vivo neutralization capacity in a humanized mouse HIV-1 model. The 2.8-Å resolution cryo-electron microscopy (cryo-EM) structure of 7-269 IgA Fab-BG505 SOSIP.664 complex showed that the 7-269 epitope is mainly composed of glycan moieties, and also revealed a germline (GL)-encoded intra-CDR_H3 disulfide bond essential for the 7-269 neutralizing activity. Thus, potent IgA bNAbs to the N332 supersite can develop in HIV-1–infected individuals, with an affinity maturation signature compatible with the one induced by vaccines, which could be essential for blocking HIV-1 mucosal transmission.

Results

Coexisting IgG and IgA bNAb lineages in HIV-1 controllers

To evaluate the neutralizing capacity of blood IgA antibodies produced by viremic controllers with broad IgG seroneutralization (n = 6), serum IgAs were purified and tested in vitro against a five-clade B-virus panel. Serum IgGs from all donors had cross-neutralizing activity, but only IgAs from patient 1 (pt1) and pt7 were able to neutralize multiple viral strains, including tier-2 viruses (Fig. 1 A and Fig. S1 A). On broader HIV-1 clade B and cross-clade reference panels (deCamp et al., 2013; Scheid et al., 2011), purified IgGs and IgAs from pt7's serum showed 46% and 33% neutralization coverage (n = 24), respectively (Fig. 1 B). To capture IgG$^+$ and IgA$^+$ B cells that could account for the serological neutralization activity in pt7, peripheral blood B cells were stained with fluorescently labeled YU2 gp140 foldon (gp140-F) or BG505 SOSIP.664 (SOSIP) trimers (Fig. 1 C). From the 364 Env-binding IgG$^+$ and IgA$^+$ memory B cells isolated by single-cell flow cytometry sorting (148 SOSIP$^+$ and 216 YU2 gp140-F$^+$), we first produced a total of 10 unique SOSIP-reactive human monoclonal antibodies by recombinant expression cloning (Prigent et al., 2016; Tiller et al., 2008; Table S1). All antibodies but one (7-216) bound both SOSIP and gp140-F proteins with various reactivity patterns and mainly recognized the gp120 subunit (Fig. S1 B). Most Env-specific antibodies were nonneutralizing or lacked neutralization activity against tier-2 viruses (Fig. S1 B). However, representative anti-gp120 antibodies from three distinct B cell lineages displayed cross-neutralizing capacity (Fig. S1 B). 7-107 antibody lineage was the most expanded and consisted only of IgA-expressing clonal members, while the 7-176 clonotype contained both IgG and IgA variants; 7-155 IgG was the sole antibody variant isolated for the third bNAb lineage (Fig. 1 D and Table S1). Other members of the 7-107 and 7-176 clonal families were also identified among gp140-F–captured memory B cells (Fig. 1 D and Table S1). 7-155 bound equally to SOSIP and gp140-F trimers, and 7-107 showed a binding preference for SOSIP, whereas 7-176 reacted with high affinity with SOSIP only (Fig. 1 E). Yet, 7-107– and 7-176–related variants pulled down with gp140-F bait (7-269 and 7-319, respectively) displayed increased relative affinity to gp140-F trimers (Fig. 1 E).

7-176, 7-155, and 7-107 neutralized 42%, 50%, and 58% of the clade B viruses tested (n = 6 tier 1, n = 6 tier 2) respectively, but were poorly active against non–clade B viral strains (Fig. 1 F and Fig. S1 C). Among gp140-F–captured pt7 bNAb variants, only 7-107–related 7-269 antibody showed enhanced neutralizing activity compared with the other lineage members (n = 10 produced in total; Fig. 1, D–G; and Fig. S1 E). 7-269 expressed as its native IgA1 subclass had IgG-equivalent profiles for HIV-1 binding and neutralization (Fig. 1 F, Fig. S1 D, and Fig. S2 A). On a cross-clade panel of viruses (n = 56), monomeric 7-269 IgA presented a neutralization breadth of 41.1%, with a geometric mean IC_{50} (half-maximal inhibitory concentration) of 0.091 µg/ml (Fig. 1 H and Fig. S1 F). Clades A (40%, n = 5), B (61%, n = 31), and C (22%, n = 9) viruses, but not clade CD/D (n = 5) or G (n = 6) viruses, were sensitive to neutralization by 7-269 IgA (Fig. 1 H and Fig. S1 F). Next, we assayed the neutralizing activity of monomeric 7-269 IgA against 38 early/transmitted HIV-1 subtype B viruses from three epidemic periods (1987–1991, 1996–2000, and 2006–2010; Bouvin-Pley et al., 2014). 7-269 IgA showed a breadth of 55.3% with a geometric mean IC_{50} of 0.146 µg/ml and a comparable neutralization profile across epidemic periods (Fig. 1 I and Fig. S1 G).

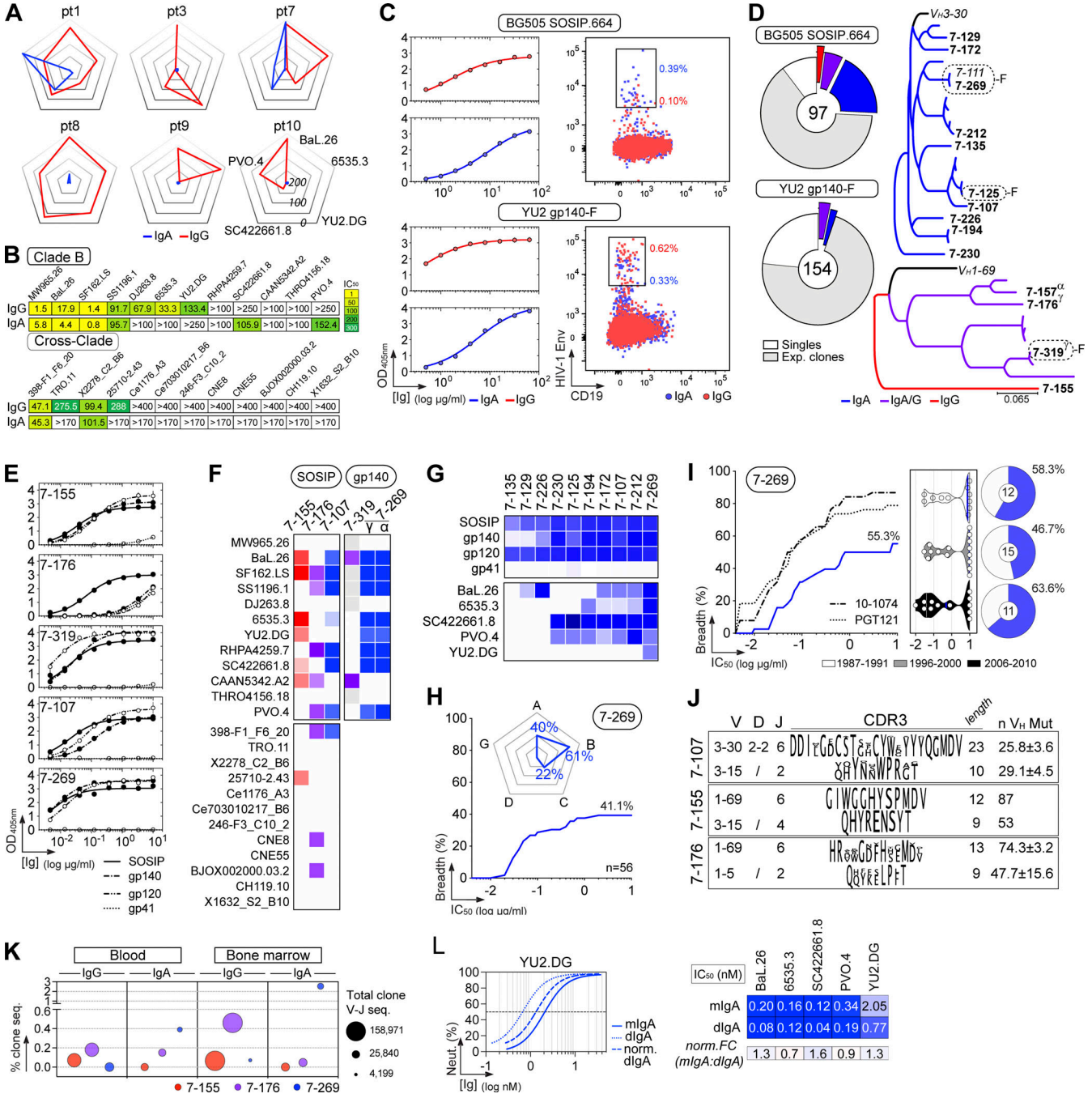

Figure 1. **Capture of broadly HIV-1 neutralizing IgG and IgA memory B cell antibodies. (A)** Radar plots comparing the in vitro neutralizing activity of IgG (red) and IgA (blue) antibodies purified from elite neutralizers' sera against a five-virus panel. **(B)** Heatmaps showing the in vitro neutralizing activity (IC_{50} in µg/ml) of purified serum IgG and IgA antibodies against two 12-virus reference panels as measured in the TZM-bl assay. **(C)** ELISA graphs (left) and flow cytometry plots (right) show the binding to BG505 SOSIP. 664 and YU2 foldon-type gp140 (gp140-F) trimers of purified serum IgG/IgA and IgG^+/IgA^+ memory B cells, respectively. OD_{405nm}, optical densities at 405 nm. Means ± SD of duplicate OD_{405nm} values are shown. **(D)** Pie charts (left) showing the distribution of unique vs. clonally expanded (Exp.) clones isolated by flow cytometric single B cell sorting using BG505 SOSIP.664 (top) and YU2 gp140-F (bottom) as baits. Colored slices indicate bNAb clonotypes for which dendrograms (right) show the relationship between clonally related IgH nucleotide sequences. Only antibodies highlighted in bold were expressed. **(E)** ELISA graphs comparing the reactivity of the selected HIV-1 bNAbs to recombinant Env proteins. Means ± SD of duplicate OD_{405nm} values are shown. **(F)** Heatmap showing the neutralization breadth and potencies of selected anti-gp160 IgG and IgA antibodies as measured in the TZM-bl assay. Means of duplicate values from two independent experiments are shown. Gray cells indicate nontested viruses with 7-319 only. **(G)** Heatmap comparing the antibody reactivity to Env proteins and neutralizing potencies of 7-107/7-269 clonal variants. **(H)** Neutralization coverage graph of 7-269 IgA bNAb against a panel of 56 viruses as measured in the TZM-bl assay. The y axis shows the cumulative frequency of IC_{50} values up to the concentration shown on the x axis. The radar plot (upper left corner) shows the frequency distribution of neutralized viruses according to HIV-1 clades. **(I)** Coverage neutralization graph (left) comparing the breadth and potency of 7-269 IgA with 10-1074 and PGT121 IgG antibodies (historical data; Bouvin-Pley et al., 2014) in the TZM-bl assay against a clade B-virus panel (n = 38) covering three periods of the HIV-1 epidemic. Violin plots (middle) show neutralization IC_{50} values for individual pseudotyped virus according to the periods of the epidemic. Pie charts (right) indicate the percentage of neutralized viruses by 7-269

per period. **(J)** Table presenting the immunoglobulin gene characteristics of the three bNAb clonotypes. n V_H Mut, number of somatic mutations in the V_H gene. **(K)** Bubble plot showing the percentage of clonal-related sequences (seq.) for the three pt7 bNAb lineages among all IgH sequences generated by Ig-HTS on DNA libraries from peripheral blood and bone marrow mononuclear cells, and filtered on bNAb-specific V-J rearrangements. **(L)** Representative graph showing the neutralizing (Neut.) activity of purified monomeric and dimeric 7-269 IgA antibodies (mIgA and dIgA, respectively) against YU2 pseudoviruses as measured in the in vitro TZM-bl assay. Means of duplicate values are shown. Heatmap (right) comparing the IC_{50} values (nM) of 7-269 mIgA and dIgA antibodies against the selected HIV-1 strains. Means of duplicate values from two independent experiments are shown as in Fig. S2 C. FC, fold-change; norm, normalized values according to the number of antibody binding sites.

7-155– and 7-176–related antibodies are encoded by V_H1-69/J_H6 and IgK (V_K3-15/J_K4 and V_K1-5/J_K2, respectively) immunoglobulin genes and harbor a 12–13-amino-acid-long CDR_H3 loop and high rates of somatic mutation at the nucleotide level (29.5% V_H/19.3% V_K and 25.1 ± 1.3% V_H/17.1 ± 5.6% V_K, respectively; Fig. 1 J and Table S1). In contrast, 7-107 bNAb variants express V_H3-30/J_H6 and V_K3-15/J_K2 gene rearrangements containing much lower hypermutation loads (8.7 ± 1.2% V_H and 10.3 ± 1.6% V_K) and possess a long CDR_H3 of 23 amino acids (Fig. 1 J and Table S1). None of the pt7 bNAb immunoglobulin genes contain nucleotide indels, except 7-176 clonotype members, which all have a 3-nucleotide deletion in their CDR_H2 loop (by Kabat definition). To further identify pt7 bNAb clonal variants, we carried out high-throughput sequencing of rearranged immunoglobulin genes separately amplified from IgG^+ and IgA^+ transcripts in blood and bone marrow B cell compartments, followed by divergence identity analyses using the bNAbs IgH sequences as references. Consistent with the data from single B cell sorting, we found clonal variants of 7-155 only in the blood and bone marrow IgG^+ cell repertoires with similar proportions, and of 7-176 among both blood and bone marrow IgA- and IgG-expressing cells, the latter being predominant (Fig. 1 K and Fig. S3 A). 7-269 clonal members were detected most exclusively in blood and bone marrow IgA^+ cell repertoires, but three close-to-GL IgG variants related to the 7-107/7-269 clonotype were also found out of the 4,199 V_H3-J_H6 total sequences from the pt7 bone marrow library (0.071%; Fig. 1 K and Fig. S3, A–C). Hypermutation-level analyses of blood and bone marrow 7-176–related IgH sequences showed that IgG^+ cells preceded the emergence of IgA^+ clonal variants (Fig. S3, A–C), suggesting a secondary class-switching event (IgM→IgG→IgA), as proposed for the M1214-N1 bNAb lineage (Jia et al., 2020). Conversely, near-GL 7-269–related IgH sequences were found among bone marrow IgG- and IgA-expressing cells, arguing in favor of an IgM B cell precursor that possibly directly switched to both IgG and IgA (Fig. S3, A–C), as shown recently for most M4008_N1 IgAs (Jia et al., 2020).

In mucosal tissues, IgA antibodies are mainly produced as J chain–containing dimeric IgA molecules (Lopez et al., 2018; Woof and Mestecky, 2015). Thus, we next purified the monomeric and dimeric IgA1 forms of 7-269 (Fig. S2 B) and compared their neutralizing activity in vitro. We found comparable IC_{50} values against the five viruses tested (Fig. 1 L and Fig. S2 C), indicating a lack of avidity effects of 7-269 IgA dimers over monomers for HIV-1 neutralization.

Antiviral potential of IgA bNAbs

To evaluate the neutralizing activity of monomeric 7-269 IgA in vivo, we generated HIV-1–infected humanized mice (hu-mice) by the engraftment of Balb/c $Rag2^{-/-}Il2rg^{-/-}Sirpa^{NOD}$ (BRGS) mice with human $CD34^+$ hematopoietic stem cells and subsequent infection with R5-tropic tier-2 NLAD8 viruses. Infected hu-mice were subjected to anti-retroviral therapy (ART) and, once aviremic, treated by a single injection of IgA antibodies (~20 mg/kg, 0.5 mg i.p. per mouse), 24 h before ART interruption. Viral rebound kinetics and intensity were assessed longitudinally by quantitative PCR of the viremia in animals receiving either 7-269 or isotype control IgA1 antibodies (Fig. 2 A). In the control group, all animals (n = 5) showed viral rebound within 2 wk after stopping ART (Fig. 2 A). In contrast, 37.5% of the mice treated with 7-269 IgA (n = 8) experienced a significant delay in viral rebound following ART cessation (P = 0.009; Fig. 2, A and B).

Next, we tested the ability of monomeric IgA bNAbs in blocking viral transcytosis across the mucosal epithelium. As previously observed with IgG bNAbs (Lorin et al., 2017), 7-157 and 7-269 IgA antibodies did not inhibit HIV-1 transcytosis through epithelial cell monolayers in vitro, but neutralized transcytosed virions (Fig. 2 C). HIV-1 Env IgG antibodies, mainly bNAbs, can exert a potent antiviral activity against HIV-1–infected target cells through antibody-dependent cellular cytotoxicity (ADCC; Bruel et al., 2016). As an ADCC prerequisite, we first examined the binding of pt7 bNAbs to target cells infected with two lab-adapted and three transmitted founder (T/F) viruses. In agreement with our previous work (Bruel et al., 2017), monomeric IgG and IgA bNAbs bound well to cells infected with lab-adapted strains but less efficiently to T/F-infected cells (Fig. 2, D and E). Accordingly, AD8-infected cell killing by primary human natural killer (NK) cells via ADCC was observed with all pt7 bNAbs binding strongly to target cells and expressed as IgGs, except for 7-155 (Fig. 2 F). In contrast, none of the IgA bNAbs expressed with their native isotype triggered NK-mediated ADCC (Fig. 2 F), in agreement with low basal surface expression of the IgA receptor CD89 on human blood NK cells (Cheeseman et al., 2016). Since HIV-1 IgA antibodies can potentially undermine IgG-mediated effector functions by interfering with Env recognition at the surface of infected cells (Ruiz et al., 2016; Tomaras et al., 2013), we tested whether IgA bNAbs could alter the ADCC activity of IgG bNAbs. 7-269 IgA blocked the reactivity of 7-319 IgG against soluble gp140-F trimers and substantially reduced its ADCC potential (18 vs. 12%, P = 0.008), while only moderately decreasing Env binding and ADCC activity of PTG128 (31 vs. 29%, P = 0.26; Fig. 2 G). Moreover, we evaluated the antibody-dependent cellular phagocytosis (ADCP) activity of pt7 IgA and IgG bNAbs using gp140-F–coated beads as particulate antigens and purified primary human monocytes as phagocytic cells expressing FcγRs and the FcαR CD89 (Fig. S4, A–C). In contrast to 10-1074 and BG8 IgG antibodies, none of the

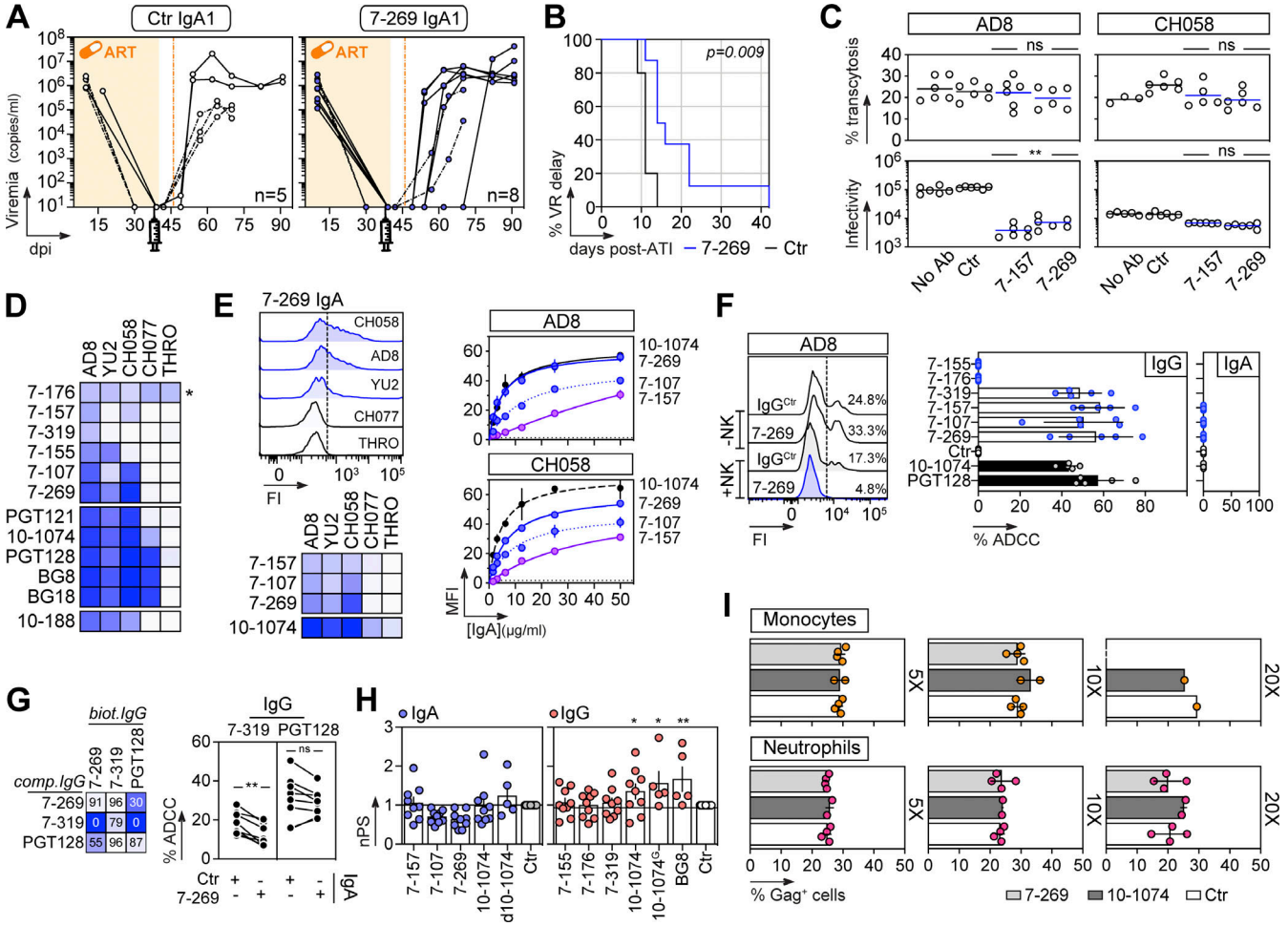

Figure 2. **In vivo neutralization and in vitro antiviral properties of 7-269 IgA bNAb. (A)** In vivo neutralization activity of human 7-269 bNAb in HIV-1–infected hu-mice. Graphs compare HIV-1 plasma viremia in ART-treated BRGS hu-mice receiving a single i.p. injection (0.5 mg) of 7-269 (n = 5) or mGO53 control (n = 8) IgA antibodies 24 h before ART interruption. **(B)** Kaplan–Meier analysis of the in vivo effect of 7-269 IgA on viral rebound (VR) following ART interruption. Groups were compared using log-rank (Mantel–Cox) test. **(C)** Dot plots comparing the percentage of transcytosis (top) and post-transcytosis infectivity (as RLU, bottom) of AD8 and CH058 virions alone (No Ab), in the presence of non–HIV-1 mGO53 control (Ctr) and 7-157 and 7-269 IgA antibodies. Mean values of triplicate values from two independent experiments are shown. Antibody groups were compared to the No Ab group using Mann–Whitney test. **, P < 0.01; ns, not significant. **(D)** Heatmap comparing the percentage of target cells infected by lab-adapted (AD8, YU2) and T/F (CH058, CH077, THRO) viruses, and bound by selected IgG antibodies (IgG⁺Gag⁺) as measured by flow cytometry. Mean values from two independent experiments are shown. **(E)** Binding of IgA bNAbs to HIV-1–infected cells. Flow cytometric histogram (top left) shows the reactivity of 7-269 IgA antibodies to Gag⁺ infected target cells. Heatmap (bottom left) shows the same as in D but for IgA antibodies. Graphs (right) show antibody binding titrations to AD8- and CH058-infected cells, measured as percentage IgA⁺ among Gag⁺ cells by flow cytometry. Mean values from two independent experiments are shown. FI, fluorescence intensity. **(F)** ADCC potential of pt7 bNAbs expressed as IgG antibodies against AD8-infected target cells. Flow cytometric histogram (left) comparing the percentage of FarRed⁺Gag⁺ cells among infected CEM.NKR cells incubated with 7-269 IgG or non–HIV-1 isotype control (mGO53, IgG^{Ctr}) in the presence of human NK cells or not. Histogram (right) comparing the percentage ADCC of AD8-infected targets incubated with selected IgG and IgA antibodies. PGT128 and 10-1074 are positive controls, and mGO53 is the negative control. Dots correspond to means of percentage ADCC values measured in duplicate for each NK-isolated human donor (n = 4 and n = 5 for IgAs and IgGs, respectively). **(G)** Competition ADCC. Heatmap (left) showing competition for ELISA binding to BG505 SOSIP.664 of selected HIV-1 bNAbs. Lighter colors indicate stronger inhibition; dark blue indicates no competition. Dot plot (right) comparing the percentage ADCC of AD8-infected targets by 7-319 and PGT128 IgG antibodies in the presence of 7-269 IgA used as competitor. Dots correspond to means of percentage ADCC values measured in duplicate for each NK-isolated human donor (n = 8). Groups were compared using two-tailed Wilcoxon test. **, P < 0.01. **(H)** Bar graphs showing the ADCP activity of selected IgA (blue) and IgG (red) antibodies expressed as normalized PS (nPS). Each dot corresponds to a healthy donor of primary monocytes (n = 4 or 8) and presents the mean of duplicate nPS values. d10-1074, dimeric 10-1074 IgA; 10-1074^{G}, 10-1074^{GASDIE} mutant antibody. Antibody groups were compared to the control (Ctr) group using two-tailed Mann–Whitney test. Only P values <0.05 are indicated: *, P < 0.05; **, P < 0.01. **(I)** Monocyte- and neutrophil-mediated ADCC potential of 7-269 IgA bNAb against AD8-infected target cells. Bar graphs comparing the percentage of FarRed⁺Gag⁺ cells among infected CEM.NKR cells incubated with 7-269 IgA1, 10-1074 IgA1, or non–HIV-1 isotype control (mGO53 IgA1, Ctr) in the presence of human monocytes or neutrophils with target:effector ratios of 1:5, 1:10, and 1:20. Each dot corresponds to a healthy donor of primary monocytes and neutrophils (up to n = 4) and presents the mean of duplicate values. P values comparing HIV-1 antibodies with the control (Ctr) using two-tailed Mann–Whitney test were not significant.

IgA and IgG bNAbs isolated from pt7 showed significant ADCP activity in vitro (Fig. 2 H). Finally, we tested the ability of 7-269 IgA to promote the elimination of HIV-1–infected cells by primary human monocytes and neutrophils (Fig. S4 D) but did not observe any reduction of the Gag$^+$ target cell frequency in the presence of monomeric IgA1 antibodies (Fig. 2 I).

Reactivity profiles of pt7 IgG and IgA bNAbs

pt7 IgA and IgG bNAbs did not bind overlapping linear peptides covering the entire consensus clade B gp120-gp41 sequence, indicating that they interact with conformational epitopes (Fig. S2 D). To map the epitopes targeted by pt7 IgG and IgA bNAbs, we first evaluated their binding to a collection of gp120 mutants by ELISA. All antibodies from the three bNAb clonotypes (7-155, n = 3 for 7-176 and n = 10 for 7-107) had decreased or abrogated binding to gp120 carrying the N332A substitution as observed for PGT135, PGT121/10-1074, and BG8/BG18 (Fig. 3 A). In addition, 7-155 and 7-176 lineage antibodies showed strong and moderate binding dependence on N386-linked glycans, respectively (Fig. 3, A and B). Apart from the potential PNGS at position N332, gp120-binding experiments also revealed interactions of 7-107/7-269 class antibodies with N295 glycan (Fig. 3, A and B). In agreement, all cross-clade panel viruses neutralized by 7-269 showed conserved N295 and N332 PNGS, while 73% of the resistant strains contained a PNGS-abrogating substitution at one of the sites (Fig. S1 F). Of note, polyclonal IgAs purified from pt7 serum, mostly monomeric, showed a slight decrease in binding to N332A-containing gp120 mutant proteins (Fig. S2, E and F). Consistent with the role of the N262 glycan in stabilizing Env (Kong et al., 2015b), all conformation-dependent antibodies showed a drastic binding reduction against gp120 N262A mutant protein (Fig. 3 A). Thus, it remains unclear whether pt7 antibodies could also interact with the N262 glycan as does PGT128 indirectly (Kong et al., 2015a). In contrast to PGT121, binding of pt7 bNAbs to a gp120 protein devoid of complex-type *N*-glycans (gp120^{kif}, produced in the presence of the mannosidase inhibitor kifunensine) was only moderately affected (Fig. 3 A). Likewise, in contrast to PGT121 and 10-1074, pt7 bNAbs still reacted strongly with gp120 with the V3 loop deleted, or bearing G324A-D325A substitutions (Fig. 3 A). To examine the contribution of Env complex-type *N*-glycans to HIV-1 neutralization, pt7 bNAbs were tested against high-mannose-only YU2 virions produced in kifunensine-treated cells. We found that the removal of complex-type *N*-glycans completely abolished 7-155 activity, while it increased the neutralizing potential of 7-269 (Fig. 3 C), suggesting that 7-269 and 7-155 mainly interact with high mannose and complex-type *N*-glycans, respectively. Next, we performed competition ELISA experiments with bNAbs of known specificity, many of them against the N332 supersite. As expected, gp120-binding cross-competition was evidenced between pt7 antibodies and with other N332-targeting bNAbs including PGT135, PGT121/10-1074, 2G12, and BG8/BG18 (Fig. 3 D). Among pt7 bNAbs, 7-269 showed the strongest competition profile (Fig. 3 D). 7-269 used as a competitor substantially decreased the binding of high-mannose patch antibodies from the same donor (7-155 and 7-176), as well as of bNAbs 2G12 and PGT135, but also of SF12, a bNAb directed against the gp120 silent face and known to make major contacts with N295 glycan (Schoofs et al., 2019).

HIV-1 gp160-specific IgG antibodies, including bNAbs to different epitopes, are frequently polyreactive and cross-reactive to self-antigens (Mouquet et al., 2010; Prigent et al., 2018). We evaluated the self-reactivity of pt7 bNAbs using a HEp-2 cell immunofluorescence assay (IFA) and human protein microarray immunoblotting. Only 7-176 presented the hallmarks for antibody auto- and polyreactivity: it bound to HEp-2 cell antigens with a cytoplasmic binding pattern (Fig. 3 E) and displayed high polyreactivity and significant cross-reactivity (Z-scores >5) to a dozen human proteins by microarray binding analyses (Fig. 3 F and Table S2). We also examined the contribution of somatic mutation to the binding and neutralizing activity of 7-269 bNAb. The putative GL precursor of 7-269 failed to bind Env proteins (Fig. 3 G) and to neutralize tier-1 and tier-2 clade B viruses (Fig. 3 H). Pairing 7-269 GL IgH with mutated IgL (7-269.IgH^{GL}) or mutated IgH with GL IgL (7-269.IgL^{GL}) did not rescue HIV-1 Env binding and neutralization. Unexpectedly, however, the hybrid antibody 7-269.IgL^{GL} retained gp120 binding and a weaker, but detectable, neutralizing activity against SC422661.8 virus (Fig. 3, G and H).

Structural characterization of the 7-269 IgA epitope

We used cryo-EM to unveil the molecular details of the 7-269 epitope. The 7-269 Fab/BG505 SOSIP.664 Env complex adopted preferential orientations on the cryo-EM grids, so we used a ternary complex with the Fab of 3BNC117, which allowed structure determination to 2.8-Å resolution (Fig. 4 A, Table S3, and Data S1). Inspection of the 7-269 interactions with the SOSIP trimer showed that, as expected, the antibody binds the high-mannose patch centered on the N332 glycan in the fourth conserved region (C4) of gp120 in the vicinity of the V3 loop stem (Fig. 4 A). In comparison with the glycan-associated V3 bNAb 10-1074, 7-269 displays a different pose on the SOSIP trimer, approaching it from the side and not from the apex (Fig. 4 B). The angle of approach of 7-269 is similar to that of 2G12, which displays a unique interlocked V_H domain–swapped dimer (Fig. 4 B), binding the opposite face of the N332 glycan with respect to 10-1074 and BG18. This binding site is too far from the GDIR motif at the base of the V3 loop to allow contacts. The structure showed that the 7-269 epitope also involves the glycan at N295 (Fig. 4, C and D), which is consistent with the binding sensitivity of 7-269 to the N332A and N295A mutations (Fig. 3, A and B), and that 7-269 makes minor contacts with gp120 protein and glycans at positions N262 and N411 (Fig. 4, C and D). The antibody's CDR_H3 penetrates deep into the cleft between the N295 and N332 glycans, reaching their base and establishing van der Waals contacts with nearby residues (Fig. 4 D). The total buried surface area (BSA) by 7-269 is ~1,600 Å^2, similar to that of other HIV-1 bNAbs (Barnes et al., 2018; Schommers et al., 2020; Seabright et al., 2020), with a predominant contribution from the heavy chain (Table S4). The BSA analysis showed that although the 7-269 paratope involves several complementarity determining regions (CDRs) and framework regions (FWRs), the CDR_H3 displays the most extensive interaction surface (>50% of the paratope's BSA; Tables S4 and S5). On the epitope side, the

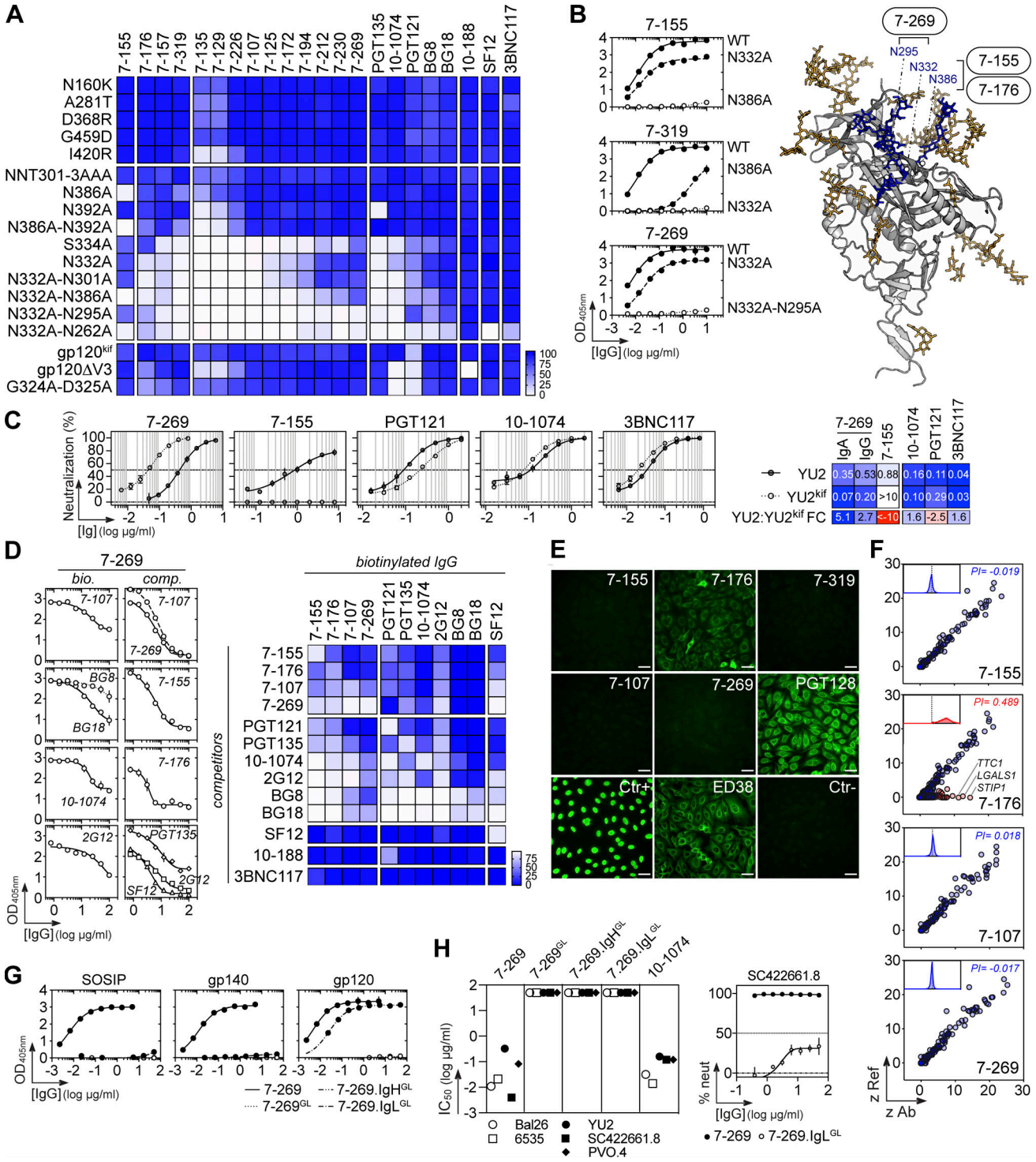

Figure 3. **Binding characteristics of coexisting IgG and IgA bNAbs. (A)** Heatmap showing the ELISA binding of selected HIV-1 bNAbs to recombinant mutant, kifunensine-treated (gp120^{kif}), V3 loop-deleted (gp120ΔV3) gp120 proteins. Color value is proportional to the reactivity level measured as percentage of binding compared to WT gp120 in at least two independent experiments. **(B)** Representative ELISA graphs (top left) comparing the binding of selected antibodies from each identified bNAb clonotypes to WT and mutant proteins carrying sensitive substitutions. Means ± SD of duplicate OD_{405nm} values from two independent experiments are shown. Ribbon diagram showing the crystal structure of glycosylated gp120 subunit (gray; glycans in orange; PDB accession no. 5T3Z), in which putative contacting glycans of prototypical bNAbs are colored in blue. **(C)** Representative graphs showing the neutralizing activity of 7-269 IgA, 7-155 IgG, and control IgG bNAbs against YU2 pseudoviruses produced in the presence of kifunensine (YU2^{kif}; dotted lines) or not (YU2; straight lines). Means ± SD of duplicate values are shown. The heatmap (right) compares the IC_{50} values (µg/ml) of the selected bNAbs against YU2 and YU2^{kif}. FC, fold-change. Mean values from two independent experiments are shown. **(D)** Competition ELISA graphs (left) comparing the binding of selected biotinylated bNAbs (-bio) in the presence of potential bNAb competitors. Means ± SD of duplicate OD_{405nm} values from two independent experiments are shown. Heatmap (right) showing competition for BG505 SOSIP.664 binding of selected HIV-1 bNAbs. Lighter colors indicate stronger inhibition; dark blue indicates no competition. **(E)** Binding

of selected HIV-1 bNAbs to HEp2-expressing self-antigens as assayed by indirect IFA. Ctr+, positive control; Ctr− and ED38 are negative and low positive control antibodies, respectively. The scale bars represent 40 µm. **(F)** Microarray plots showing the reactivity of selected HIV-1 bNAbs to human proteins. Each spot corresponds to the z-scores given on a single protein by the reference antibody (Ref: mGO53, y axis) and test antibody (x axis). Red dots indicate immunoreactive proteins (z > 5) presented in Table S2. Frequency histograms in the upper left corner show the $\log_{10}$ protein displacement (σ) of the MFI signals for HIV-1 bNAbs compared to nonreactive antibody mGO53. The PI corresponds to the Gaussian mean of all array protein displacements. **(G)** ELISA graphs comparing the binding to Env proteins of the selected bNAbs, GL, and mutated-GL hybrid counterparts. Means ± SD of triplicate OD_{405nm} values are shown (representative of three independent experiments). **(H)** In vitro neutralizing activity of mutated, GL, and hybrid versions of 7-269 bNAb. Dot plot (left) comparing the IC_{50} values for the neutralization of clade B viruses (n = 5) as determined in the TZM-bl assay. 10-1074 and 7-269 are positive controls. Neutralization graph (right) shows the neutralizing activity of 7-269 and 7-269.IgL^{GL} against SC422661.8. Means ± SD of duplicate IC_{50} values are shown (representative of three independent experiments).

N332 glycan contributes to the largest contact area, involving almost all its glycan moieties except for those on the D2 arm (Tables S4 and S5). In contrast, gp120-interacting residues represented only 13% of the epitope's BSA (Tables S3 and S4). The 7-269 residues interacting with the N332 and N295 glycans are on opposite faces of the Fab, while the residues in contact with the N262 and N411 glycans are on each side (Fig. 4 E). The few residues that contact the gp120 protein (H109, Y114, and Y115) are at the CDR_H3 tip (Fig. 4 E and Fig. S5 E). Binding is favored by hydrogen bonds that exclusively involve glycans (at positions N295, N332, and N262; Fig. S5), while 7-269/gp120 contacts with protein residues are mediated by van der Waals interactions only (Fig. 4 E and Fig. S5 E). The absence of polar interactions with the Env protein is another commonality between 7-269 and 2G12, besides similar angles of approach and no contacts with the GDIR motif. Since 7-269 is able to penetrate deep into the glycan shield, it contacts protein residues at the base of the glycans (N295, N332, S334, N411, D412, and S413; Fig. 4 D and Fig. S5 E). The sole residues contacted by 7-269 that are not associated with a glycosylation sequon are R444, which faces H109 from the CDR_H3 loop, and V446 (Fig. S5 E).

As mentioned above, 7-269 CDR_H3 contributes to the largest contact area as well as key polar interactions with the SOSIP trimer. Long CDR_H3s in bNAbs targeting the glycan-associated variable loops can adopt different shapes: protruding with a two-stranded β-hairpin, e.g., 3H+109L (Garces et al., 2015), PGT121, and 10-1074 (Mouquet et al., 2012; Fig. 4 F), or with an extended configuration as in BG18 (Barnes et al., 2018; Fig. 4 F), while others have an elongated U-shaped loop as in 438-B11 (Kumar et al., 2020; Fig. 4 F). 2G12 is an exception, since it harbors a short CDR_H3 that is compensated by swapped V_H domains extending its interaction surface (Calarese et al., 2003; Fig. 4 F). Instead of protruding or adopting an elongated conformation, the long CDR_H3 of 7-269 (23 residues) presents several turns, shaping it as a shamrock or a light bulb filament (Fig. 4, F and G). Another relevant feature of the 7-269 CDR_H3 is a disulfide bond formed between Cys^{105} and Cys^{110} (Fig. 4, F and G; and Fig. S5). Intra-CDR_H3 disulfide bonds have been described in only a handful of HIV-1 bNAbs, including the anti-V1V2 CAP256-VRC26.03 (Doria-Rose et al., 2014), the anti-V3-glycan 438-B11 (Kumar et al., 2020), and a few anti-CD4bs antibodies from the VRC01 lineage (Wu et al., 2015; Fig. 4 G). The disulfide bond formed in the CDR_H3 of 7-269 via a CX_4C motif is encoded by GL nucleotides of the D_H2-2 segment (Prabakaran and Chowdhury, 2020) and is well conserved in all clonal members of its lineage (Fig. 1 J, Fig. S3 D, and Table S1). To examine the functional contribution of the C105-C110 bond, we produced single and double cysteine-mutant antibodies preventing its formation in 7-269 (7-269.IgH^{C105A} and 7-269.IgH$^{C105A\text{-}C110A}$). 7-269.IgH^{C105A} and 7-269.IgH$^{C105A\text{-}C110A}$ IgGs and IgAs showed decreased relative affinities to HIV-1 Env proteins compared with the parental 7-269 antibodies (Fig. 4 H), which translated into a complete loss of neutralizing activity against three of the five virus strains tested (Fig. 4 I). Thus, the GL-encoded intra-CDR_H3 disulfide bond is a key molecular element conferring glycan contacts in the high mannose patch and cross-neutralizing properties.

All pt7 bNAbs target the N332 glycan supersite

To better understand the basis of pt7 bNAbs' cross-competition and delineate 7-155 and 7-176 epitopes, we determined cryo-EM single-particle reconstructions of the BG505 SOSIP.664 trimer in complex with 7-155 and, separately, with 7-176 IgG Fab at a resolution of 6.7 and 7.0 Å, respectively (Fig. 5, A and B; and Data S2). As a crystal structure of the isolated Fabs was not available, we used homology models of the 7-155 and 7-176 Fabs to interpret the cryo-EM maps, mainly for identifying key interacting glycans on gp120. Fitting of the Fab variable domains indicated that 7-155 is far from the N295 glycan and in proximity to the V1 loop and the N332, N386, and N392 glycans (Fig. 5 C). Similarly, 7-176 is also far from the N295 glycan and close to the N332, N386, and N392 glycans (Fig. 5 D). This is in agreement with our gp120 binding data showing sensitivity of 7-155 and 7-176 antibodies to N332A and N386A mutations (Fig. 3, A and B). Of note, both cryo-EM reconstructions are compatible with Env interactions established exclusively by the heavy chain, without contacts between the light chain and the SOSIP trimer. Superposition of the 7-155, 7-176, and 7-269 complexes on the SOSIP moiety showed that all bNAbs target the N332 high-mannose patch, providing a mechanistic explanation for their strong competition for binding (Fig. 5 E). The 7-155 and 7-176 epitopes are away from the GDIR motif at the base of the V3 loop (Fig. 5, C and D), indicating that pt7 bNAbs share a particular binding mode in which the engagement of the N332 high-mannose patch does not involve the GDIR motif. Despite those common characteristics, the antibodies present differences in terms of their binding orientations: 7-269 binds with a horizontal V_HV_L plane, perpendicular to the Env threefold axis, whereas the V_HV_L plane in the 7-155 and 7-176/SOSIP complexes is diagonal (Fig. 5 E). As a consequence, 7-269 binds the face of the gp120 protomer containing the N295 glycan, whereas the 7-155 and 7-176

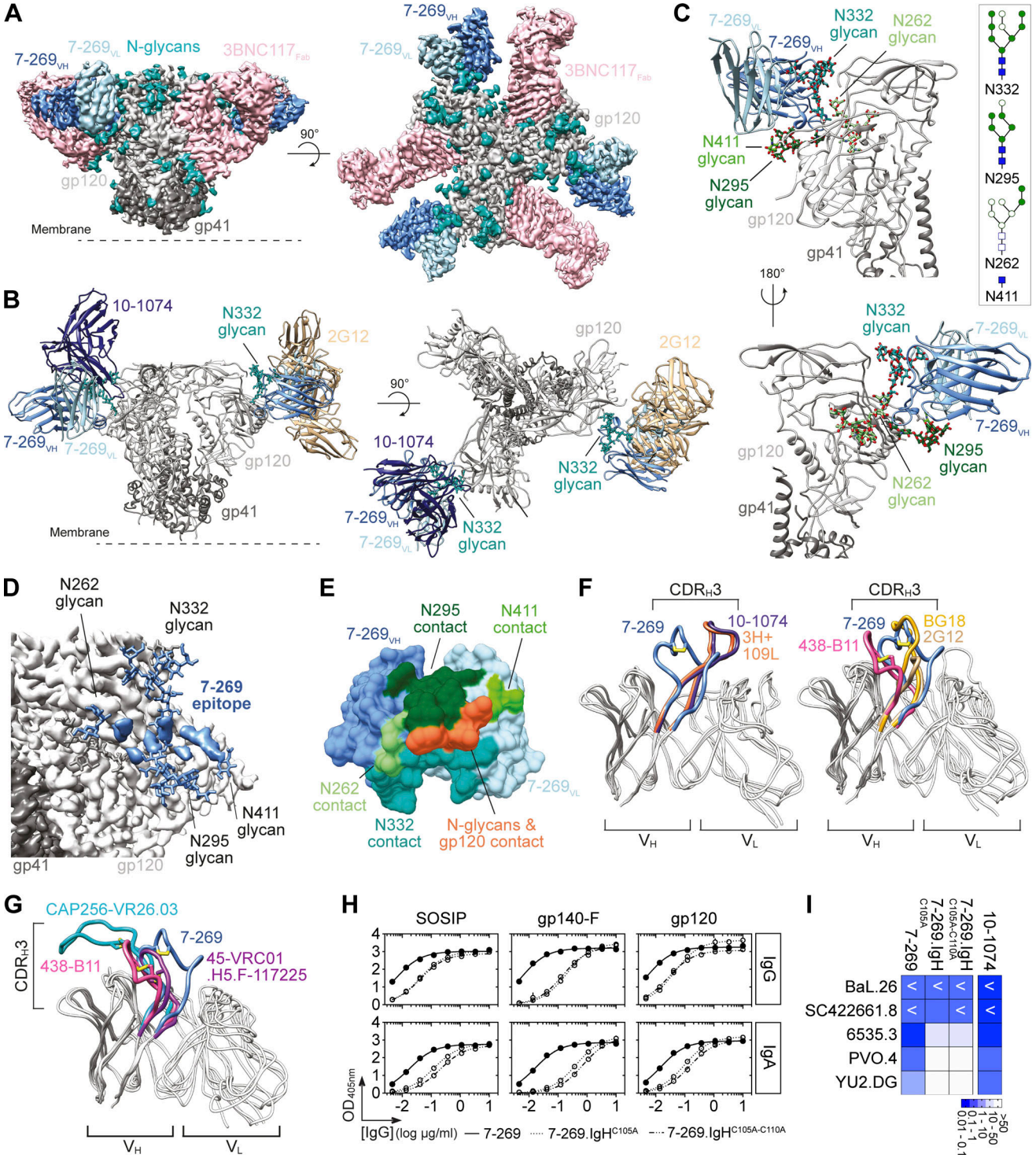

Figure 4. **Structural analyses of the BG505 SOSIP.664-7-269 IgA Fab complex. (A)** Side view (left) and top view (right) of the 2.8-Å single-particle cryo-EM reconstruction of the BG505 SOSIP.664-7-269-3BNC117 complex colored by components (dark gray, gp41; light gray, gp120; blue, 7-269 V_H; light-blue, 7-269 V_L; pink, 3BNC117 Fab; green, *N*-glycans). **(B)** Structure of the BG505 SOSIP.664-7-269 complex with other anti-glycan V3 bNAbs superimposed. One protomer was aligned to gp120 in the complex with 10-1074 (PDB accession no. 5T3Z), while another protomer was superimposed to the structure of the Env with 2G12 (PDB accession no. 6OZC). Only the variable heavy and light chains are shown, and the N332 glycan is indicated (green). **(C)** Structure of the HIV-1 Env-7-269 protomer highlighting in sticks the glycans that establish major (N295 and N332) and minor (N262, N411) contacts with the antibody. The inset in the top right corner presents the glycan residues modeled at each position, indicating with filled symbols those in contact with 7-269. Squares and circles represent *N*-acetylglucosamine and mannose residues, respectively. **(D)** Mapping of the 7-269 epitope (colored in blue) on the density from the EM map corresponding to the BG505 SOSIP.664 trimer. The glycans in the interface are shown in sticks, with the sugar residues forming the epitope in blue. **(E)** Surface representation of the 7-269 variable domains with residues contacting a particular glycan (or glycan and gp120) indicated in the same color. **(F)** Structural superposition of the IgH and IgL variable domains (V_H and V_L, respectively) from 7-269 and anti-glycan-V3 bNAbs that have either a protruding CDR_H3 with a

β-hairpin (left; 10-1074 [PDB accession no. 5T3Z] and 3H+109L [PDB accession no. 5CEZ]) or an extended or short CDR_H3 (438-B11 [PDB accession no. 6UUH], BG18 [PDB accession no. 6CH7], and 2G12 [PDB accession no. 6OZC]). **(G)** Structural superposition of the variable domains from 7-269 and anti-HIV bNAbs harboring an intra-CDR_H3 disulfide bond (yellow sticks) and targeting the glycans-V3 (438-B11 [PDB accession no. 6UUH]), glycans-V1/2 (CAP256-VR26.03 [PDB accession no. 4OD1]), and the CD4bs (45-VRC01.H5.F-117225 [PDB accession no. 4S1S]). **(H)** ELISA graphs comparing the Env binding of 7-269 and associated CDR_H3 cysteine mutant antibodies. Means ± SD of duplicate OD_{405nm} values are shown (representative of two independent experiments). **(I)** Heatmap comparing the neutralizing activity of 7-269 and associated CDR_H3 cysteine mutant antibodies as measured in the TZM-bl assay. Representative data of two independent experiments are shown. <, IC_{50} below the depicted value.

epitopes expand along the N332 glycan and the opposite face of gp120 (Fig. 4 and Fig. 5). Collectively, the structural information indicates that although pt7 bNAbs target the same N332 supersite, also known as the high-mannose patch, the binding angles and glycan recognition patterns are unique to this category of bNAbs.

Discussion

Up to now, investigations on HIV-1 bNAbs have been exclusively focused on IgG antibodies. Env-specific IgA antibodies are elicited in response to HIV-1 infection (Lopez et al., 2018; Nabi et al., 2017; Ruiz et al., 2016) but remain understudied despite their functional relevance (Black et al., 1996; Lopez et al., 2018;

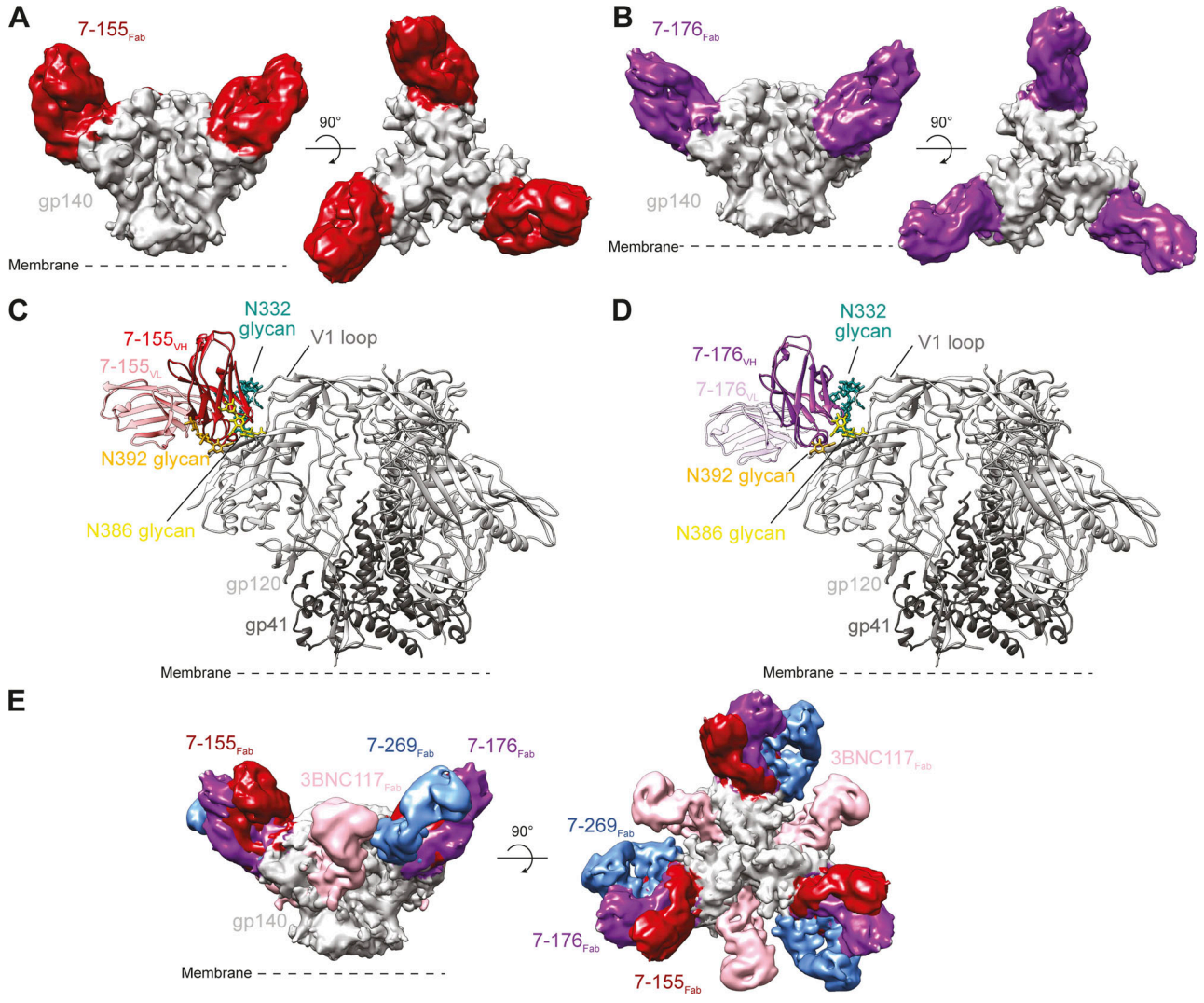

Figure 5. **Cryo-EM structures of 7-155 and 7-176 in complex with BG505 SOSIP.664 trimer. (A)** Side view (left) and top view (right) of the 6.7-Å single-particle cryo-EM reconstruction of HIV-1 BG505 SOSIP.664 Env in complex with 7-155 IgG Fab. **(B)** Same as in A but for the 7.0-Å cryo-EM reconstruction of Env-7-176-IgG Fab complex. **(C)** Model of the BG505 SOSIP.664-7-155 complex (side view) obtained by fitting the BG505 SOSIP.664 structure and homology models from the antibodies' variable regions and the BG505 SOSIP.664 structure into their respective single-particle reconstructions. The glycosylated BG505 SOSIP.664 structure was taken from the complex with 7-269, and some mannose residues were trimmed to avoid clashes with the modeled antibody. **(D)** Same as in C but for BG505 SOSIP.664-7-176 complex. **(E)** Superposition of the reconstructions obtained for the three BG505 SOSIP.664-bNAb complexes studied (side and top views), showing the overlap between their respective binding sites. For a better comparison, the data from the BG505 SOSIP.664-7-269-3BNC117 complex was reprocessed with a resolution limit of 7 Å.

Mouquet, 2014; Planque et al., 2010; Wills et al., 2018). Here, we report on the characterization of IgA bNAbs isolated from a viremic controller with broad seroneutralization. HIV-1 strain-specific IgA monoclonal antibodies have been previously cloned from the blood and/or intestinal B cells of infected individuals and RV144 vaccinees, but showed no heterologous cross-neutralization (Bonsignori et al., 2017; Gray et al., 2011; Planchais et al., 2019; Tomaras et al., 2013; Trama et al., 2014; Wills et al., 2018). It is only recently, however, that the first naturally occurring IgA bNAbs have been isolated using Env-containing viral particles (Jia et al., 2020). It has been postulated that the paucity of recovered IgA bNAb-expressing B cells could originate from the inappropriate use of soluble recombinant Env proteins as baits (Magri and Cerutti, 2020). A more plausible alternative resides in inadequate strategies to purposely identify circulating IgA bNAbs, which would require to (i) screen for IgA-mediated seroneutralization, (ii) capture single Env-reactive IgA^+ B cells, and (iii) amplify immunoglobulin genes from IgA transcripts. Using this rational approach in a viremic controller (pt7) with serum IgA cross-neutralization, we isolated numerous IgA bNAb variants from two distinct B cell lineages using SOSIP and gp140 foldon-type recombinant trimers as probes. We also discovered a third bNAb lineage in pt7, represented by a unique IgG member. Cross-neutralizing serum IgA antibodies were detected in only a third of the Elite neutralizers screened here. This observation suggests that IgA bNAbs may develop more rarely than their IgG counterparts. Nonetheless, greater numbers of infected individuals with serum cross-neutralization, including Elite neutralizers, need to be investigated to clarify the contribution of IgA antibodies to seroneutralization. Strikingly, epitope mapping showed that all pt7 IgA and IgG bNAbs target the high-mannose patch centered on the N332 glycan without interacting with the V3 loop base, which contrasts with numerous bNAbs to the N332 supersite (Daniels and Saunders, 2019). The structural data confirmed this observation and further revealed two other specific features of 7-269 IgA: an intra-CDR_H3 disulfide bond and a 2G12-type Env binding approach. Intra-CDR disulfide bonds can be found in antibodies targeting viral antigens including HIV-1 Env (Prabakaran and Chowdhury, 2020), where they often stabilize and rigidify long CDR_H3 loops. Intra-CDR_H3 disulfide bonds in HIV-1 bNAbs are functionally important, as shown for the anti-V3 glycan antibody 438-B11, in which disulfide bond disruption reduces its affinity and neutralizing activity (Kumar et al., 2020). Likewise, we showed that the disulfide bond in the 7-269 CDR_H3 loop is pivotal for HIV-1 binding and neutralization. Interestingly, 7-269 shares several binding characteristics with 2G12, including an epitope mainly made of sugar residues (~90% of the epitope's BSA) comprising those at position N332 and N295, no or very minor contacts with the protein moiety, and the angle of approach to the N332 supersite (Seabright et al., 2020). Thus, despite 2G12 being a special class of antibody with a unique V_H domain–swapped paratope, more potent, normal IgA and IgG bNAbs targeting the same site and with a similar angle of approach can develop in HIV-1–infected individuals. B cell lineages of IgG bNAbs targeting overlapping or distinct neutralizing sites can co-exist in Elite neutralizers including viremic controllers (Freund et al., 2017; Gao et al., 2014; Klein et al., 2012; Krebs et al., 2019; Longo et al., 2016; Scheid et al., 2011). Two co-existing lineages of bNAbs with narrow breadth and potency (N170-VRC22 and N170-VRC29), but showing N332 and/or N301 glycans-dependent Env binding were previously identified in an Elite neutralizer (Longo et al., 2016). bNAb B cell lineage co-evolution with diversifying viruses can occur through cooperative mechanisms between bNAb and/or strain-specific "helper" lineages (Anthony et al., 2017; Gao et al., 2014). Whether bNAbs-initiating viruses displayed attributes facilitating exposure to the N332 supersite, and whether B cell lineages that developed in pt7 cooperated to overcome viral escape, could not be addressed here. Yet, the 7-107/7-269 clonotype emerged last based on hypermutation as a molecular clock for B cell evolution, which suggests that pre-existing lineages recognizing overlapping N332-supersite epitopes (7-155 and 7-176) could have played a role in its genesis. In the absence of detailed longitudinal analyses on pt7's donor, it also remains unclear whether IgG bNAb precursors preceded or coemerged with IgA antibody variants. Class-switching has been proposed as a potential redemption mechanism of B cell clones; as a result, IgA1 can have enhanced neutralization properties against autologous viruses compared with IgG1 (Scheepers et al., 2020). Coexisting IgA^+ and IgG^+ memory B cell clones with identical variable domains were not isolated from pt7 precluding an unbiased comparative neutralization analysis. Of note, however, we did observe comparable HIV-1 binding and neutralizing activity of 7-269 when expressed as IgG and IgA antibodies against heterologous viruses, indicating that IgG-to-IgA class-switching does not substantially modulate 7-269 antigen-binding sites as previously shown for other bNAbs (Lorin et al., 2017).

Remarkably, 7-269 IgA displayed only 9.1 and 9.5% somatic mutation in V_H3-30 and V_K3-15 genes, respectively (corresponding to ~15% amino acid changes), without indels, and still achieved ~50% neutralization breadth. In line with this observation, among bNAb B cell lineages harboring the lowest hypermutation loads already described in infected infants and adults, most target high-mannose patch epitopes (Bonsignori et al., 2017; Krebs et al., 2019; Kumar et al., 2019; MacLeod et al., 2016; Simonich et al., 2016). Such low-to-moderate levels of somatic mutation in bNAbs are likely to be more compatible with their induction by vaccines, as they would require simpler vaccination regimens spanning reasonable time periods. Hence, rationally designed immunogens and immunization strategies to elicit neutralizing antibodies against the N332/V3 loop supersite hold promise for developing effective HIV-1 vaccines (Moyo et al., 2020). The induction of IgA bNAbs in mucosa-associated lymphoid tissues could indeed greatly contribute to preventing sexual transmission of HIV-1. Indeed, we showed that 7-269 IgA was able to delay viral rebound in vivo in humanized mice and to neutralize HIV-1 virions crossing the mucosal epithelium in vitro. While mucosal sites generate higher levels of J chain–associated IgA dimers, they also produce monomeric IgAs (Lopez et al., 2018; Woof and Mestecky, 2015). Whether the monomeric IgA1 bNAbs we described developed in the gut of pt7 donor or elsewhere in mucosa-associated lymphoid tissues remains unclear. Current candidate vaccines appear

inefficient at generating mucosal IgAs to HIV-1 Env (Seaton et al., 2021), indicating that novel strategies are required to guide the production of protective antibodies in mucosa. Viral neutralization is mandatory to efficiently block viral transmission at mucosal sites (Astronomo et al., 2016; Cheeseman et al., 2017; Lorin et al., 2017). To elicit mucosal bNAbs while minimizing immune diversion phenomena of gut humoral responses to HIV-1 (Trama et al., 2014; Williams et al., 2015; Planchais et al., 2019), bNAb lineage-based vaccine approaches should therefore be employed (Kwong and Mascola, 2018). Fc-dependent antiviral activities of bNAbs may also help limiting transmission events at mucosal surfaces (Santra et al., 2015). HIV-1 Env-specific IgA antibodies with ADCP and/or ADCC activity have been previously reported (Black et al., 1996; Duchemin et al., 2018; Duchemin et al., 2020; Tay et al., 2016; Wills et al., 2018) but may be less potent effectors than their IgG counterparts (Tay et al., 2016). Here, we found that pt7-derived IgA bNAbs lacked ADCC and ADCP potential in vitro, whereas IgGs promoted NK-mediated elimination of infected cells, as shown for other N332 supersite-targeting bNAbs (Bruel et al., 2016; Bruel et al., 2017). Thus, the specificity of pt7 IgAs is likely not accountable for their apparent lack of activity, which may rather be linked to either effector immune cells or Fc–FcαR interactions. In fact, IgA effector functions are known to depend on immunoglobulin subclass, Fc glycosylation, and isoform status, with monomeric IgAs and the IgA1 isotype being less effective (Gayet et al., 2020; Steffen et al., 2020). In contrast, we showed that epitope-overlapping IgA antibodies could partially block the ADCC activity of IgGs to the N332 supersite as previously reported for IgAs targeting the gp120 first constant (C1) region (Tomaras et al., 2013). Whether pt7 IgA antibodies could nonetheless cooperate at a polyclonal level with non–N332-specific anti-Env IgGs to promote Fc-dependent elimination of infected cells, as proposed for RV144 vaccine-induced antibodies (Fischinger et al., 2020), remains unclear. Hence, further investigations are needed to precisely define the parameters influencing Fc-dependent effector functions of HIV-1 Env-specific IgA antibodies.

In summary, our results show that multiple bNAb B cell lineages combining IgG and IgA antibodies and converging toward a single epitopic Env region can codevelop in HIV-1–infected individuals undergoing viremic control. Our data also revealed singular characteristics of novel genuine IgA bNAbs extending the current knowledge on the neutralizing humoral response to HIV-1, with important implications for immunogen design and vaccine development.

Materials and methods

Human samples

Samples were obtained as part of the BHUANTIVIH clinical research protocol, which was performed in accordance with and after ethical approval from the Institutional Review Board of the Institut Pasteur (CoRC#2013-21), and all the French legislation and regulation authorities. Peripheral blood mononuclear cells (PBMCs), bone marrow mononuclear cells, and sera were collected at the Laboratory of Molecular Immunology at the Rockefeller University as part of the MNU-0628 protocol, which received ethics approval from the Institutional Review Board of the Rockefeller University (#320609). The BHUANTIVIH protocol received approval from the Comité Consultatif pour le Traitement de l'Information en matière de Recherche dans le domaine de la Santé on December 12, 2013 (#13.775), and the Commission Nationale de l'Informatique et des Libertés on August 8, 2014 (#DR-2014-313). All donors gave written consent to participate in this study. Ethical issues have been monitored by the Ethics Board for European contracts, an ad hoc independent Ethics Committee in charge of periodically reviewing sensitive ethical issues in European Union–funded research when requested by the European Union. pt7 donor (male) was 32 yr old at sampling time (13 yr after diagnosis), with a blood $CD4^+$ count of 430 cells and a blood viral load of 505 copies/ml. Human IgG and IgA antibodies were purified from donors' sera by affinity chromatography using Protein G Sepharose 4 Fast Flow (GE Healthcare) and peptide M-coupled agarose beads (InvivoGen), respectively. Purified serum antibodies were dialyzed against PBS using Slide-A-Lyzer Cassettes (30K MWCO; Thermo Fisher Scientific). Human peripheral whole blood samples and buffy coats from healthy donors were obtained at the Etablissement Français du Sang.

HIV-1 Env proteins

HIV-1 antigens: for YU2 gp120 mutant proteins, single point mutations were introduced into the pYU2 gp120 expression vector (gift of J. Sodroski, Harvard Medical School, Boston, MA) using the QuickChange Site-Directed Mutagenesis kit (Agilent Technologies) following the manufacturer's instructions. Site-directed mutations were verified by DNA sequencing. His- and Avi-tagged clade B YU2 gp140 (Yang et al., 2000) and BG505 SOSIP.664 (Sok et al., 2014) trimers, YU2 gp120, V3 loop-deleted (ΔV3; Mouquet et al., 2012), and mutant proteins were produced by transient transfection of exponentially growing Freestyle 293-F suspension cells (Thermo Fisher Scientific) using polyethylenimine (PEI) precipitation method, purified by high-performance chromatography using the Ni Sepharose Excel Resin according to manufacturer's instructions (GE Healthcare), and controlled for purity by SDS-PAGE and NativePAGE gel staining as previously described (Lorin and Mouquet, 2015). For BG505 SOSIP.664 production, Freestyle 293-F cells were co-transfected with a furin-encoding pcDNA3.1 vector (at a SOSIP/furin ratio of 4:1). High-mannose-only YU2 gp120 protein was produced in HEK-293T cells treated with 25 μM kifunensine (Enzo Life Sciences; Mouquet et al., 2012). Anti-V1-V2/glycans PGT145 (Walker et al., 2011) produced and purified as described below was coupled to NHS-activated Sepharose 4 fast flow gel beads (GE Healthcare) as previously described (Lorin and Mouquet, 2015) using 10 mg of purified IgG per 1 ml of beads, and PGT145-coupled resin (4 ml) was then packed in an empty XK16 column between two adaptors after extensive washes with PBS. BG505 SOSIP.664-containing supernatant was loaded at a flow rate of 1 ml/min (both directions) onto the PGT145-coupled resin, which was then washed with 10 CV of buffer (0.5 M NaCl and 20 mM Tris, pH 8.0) at a flow rate of 1 ml/min. BG505 SOSIP.664 proteins were eluted by fractionation with 20 CV of 3 M $MgCl_2$ at a flow rate of 1 ml/min. Protein fractions were

pooled, dialyzed against 75 mM NaCl and 10 mM Tris, pH 8.0 (10K MWCO Slide-A-Lyzer dialysis cassettes; Thermo Fisher Scientific), and concentrated using a Amicon Ultra-4 centrifugal filter unit (10K MWCO; Millipore). YU2 gp140 and BG505 SOSIP.664 trimers were then purified by fast protein liquid chromatography (FPLC)/size exclusion chromatography (SEC) using an AKTA pure FPLC instrument (GE Healthcare) with a Superdex 200 increase 10/300 GL or HiLoad 16/600 Superdex 200 pg column (GE Healthcare) following the procedure described previously (Lorin and Mouquet, 2015). Final protein concentrations were measured using a NanoDrop 2000 instrument (Thermo Fisher Scientific). The purity of the Env trimers was evaluated by SDS-PAGE using 4–12% Bis-Tris Novex gels (Life Technologies) in nonreducing and nondenaturing conditions, and by native PAGE using NativePAGE Novex 3–12% Bis-Tris gels followed by in-gel protein silver staining (Silver Stain kit; Thermo Fisher Scientific). YU2 gp140-F and BG505 SOSIP.664 trimers used for B cell FACS capture were biotinylated using BirA biotin-protein ligase bulk reaction kit (Avidity). Purified clade B MN gp41 protein (#12027) and consensus clade B 15-mer overlapping peptide library (#9480) were provided by the National Institutes of Health (NIH) AIDS Reagent Program.

Antibody controls

Human HIV-1 IgG antibodies used as reference controls are as follows: anti-V3^{crown} 10-188 (Mouquet et al., 2011); bNAbs 2G12 (Trkola et al., 1996), anti-CD4bs 3BNC117 (Scheid et al., 2011), anti-V3-glycan PGT121, PGT135, 10-1074, and BG8/BG18 (Freund et al., 2017; Mouquet et al., 2012; Walker et al., 2011); and anti-silent face SF12 (Schoofs et al., 2019). Non–HIV-1 antibodies include polyreactive and nonpolyreactive antibody ED38 (Meffre et al., 2004) and mGO53 (Wardemann et al., 2003), respectively. 10-1074 and mGO53 IgA monoclonal antibodies were also generated (Lorin et al., 2017). Recombinant IgG and IgA antibodies were produced by cotransfection of Freestyle 293-F cells (Thermo Fisher Scientific) using PEI precipitation method as previously described (Lorin and Mouquet, 2015; Tiller et al., 2008) and purified by affinity chromatography using protein G Sepharose 4 fast flow beads (GE Healthcare) and peptide M-coupled agarose beads (InvivoGen), respectively. For competition ELISA experiments, purified antibodies were biotinylated using the EZ-Link Sulfo-NHS-Biotin kit (Thermo Fisher Scientific).

Human primary cell isolation

PBMCs were isolated from donors' blood products using Ficoll Plaque Plus (GE Healthcare). Monocytes and NK cells were isolated from donors' PBMCs by magnetic cell sorting using human CD14 microbeads and NK cell isolation kit, respectively (Miltenyi Biotec). Neutrophils were isolated from donors' fresh blood using the MACSxpress whole blood neutrophil isolation kit (Miltenyi Biotec) following the manufacturer's instructions. To check purity, cells were first stained for 30 min at 4°C with LIVE-DEAD fixable aqua dead cell stain kit (for 405-nm excitation; Invitrogen Thermo Fisher Scientific). Human monocytes and neutrophils were then stained for 10 min at room temperature with, respectively, PE anti-human CD14 and APC anti-human CD16, and FITC anti-human CD15 and APC anti-human CD16 (Miltenyi Biotec). Before the ADCC assay, purified NK cells were cultured overnight at 37°C in 10% FCS-RPMI 1640 supplemented with 1% penicillin (10,000 U/ml)/streptomycin (10,000 µg/ml; Fisher Scientific). FcγR and FcαR expression on isolated cells was evaluated by flow cytometric staining with APC anti-human CD16 (clone REA423; Miltenyi Biotec), BV421 anti-human CD89 (clone A59; BD Biosciences), FITC anti-human CD64 (clone 10.1; Invitrogen), and human anti-CD32a antibody MDE8 (van Royen-Kerkhof et al., 2005) coupled to DyLight 594 (Thermo Fisher Scientific). Data on stained cells were acquired using a BD LSR Fortessa cytometer (BD) and analyzed using FlowJo software (v10.7.1).

Single B cell FACS sorting and expression cloning of antibodies

Peripheral blood human B cells were isolated from pt7's PBMCs by CD19 MACS (Miltenyi Biotec) and stained with LIVE-DEAD fixable dead cell stain kit (Thermo Fisher Scientific). Purified B cells were then incubated for 30 min at 4°C with biotinylated recombinant YU2 gp140-F or BG505 SOSIP.664 trimers (1 µg/ml), washed with 1% FBS-PBS (FACS buffer), and incubated for 30 min at 4°C with a cocktail of mouse anti-human antibodies CD19 AF700 (HIB19; BD Biosciences), CD27 PE-CF594 (M-T271; BD Biosciences), CD21 BV421 (B-lyA; BD Biosciences), IgM BV605 (G20-127; BD Biosciences), IgG BV786 (G18-145; BD Biosciences), IgA FITC (IS11-8E10; Miltenyi Biotec), and streptavidin R-PE conjugate (Thermo Fisher Scientific). Stained cells were washed and resuspended in 1 mM EDTA FACS buffer. Single S-Env$^+$CD19$^+$IgG$^+$/IgA$^+$ B cells were sorted into 96-well PCR plates using a FACS Aria III sorter (BD) as previously described (Tiller et al., 2008). Single-cell cDNA synthesis using SuperScript IV reverse transcriptase (Thermo Fisher Scientific) followed by nested-PCR amplifications of IgH, Igκ, and Igλ genes, and sequence analyses for Ig gene features were performed as previously described (Prigent et al., 2016; Scheid et al., 2011; Tiller et al., 2008). For the reversion to GL of the selected antibodies, sequences were constructed by replacing the mutated V_H-(D_H)-J_H and V_L-J_L gene segments with their GL counterparts as previously described (Mouquet et al., 2012). Purified digested PCR products were cloned into human Igα1-, Igγ1-, Igκ-, or Igλ-expressing vectors as previously described (Lorin and Mouquet, 2015; Tiller et al., 2008). Recombinant antibodies were produced by transient cotransfection of Freestyle 293-F suspension cells (Thermo Fisher Scientific) using PEI precipitation method as previously described (Lorin and Mouquet, 2015). Recombinant human IgG and IgA antibodies were purified by affinity chromatography using Protein G Sepharose 4 Fast Flow (GE Healthcare) and peptide M-coupled agarose beads (InvivoGen), respectively. Monomeric and J-chain-containing dimeric 7-269 IgA antibodies were produced and purified by peptide M-based affinity chromatography followed by SEC-based FPLC as previously described (Lorin and Mouquet, 2015). Purified antibodies were dialyzed against PBS. Preparations for in vivo infusions were microfiltered (Ultrafree-CL devices; 0.1-µm PVDF membrane; Merck-Millipore) and checked for endotoxin levels using the ToxinSensor Chromogenic LAL Endotoxin Assay Kit (GenScript).

High-throughput immunoglobulin repertoire sequencing

Total mRNAs were extracted from PBMCs and bone marrow cells using Nucleospin RNA kit and Nucleospin RNA XS kit (Macherey Nagel), respectively. cDNAs were generated from 0.5–1-µg mRNAs using random hexamers (pd(N)6; Roche) and SuperScript IV reverse transcriptase (Thermo Fisher Scientific) following the manufacturer's protocol. IgG and IgA DNA fragments were first amplified from 5 µl of cDNA using 2 U of Platinum Taq DNA polymerase (Thermo Fisher Scientific) according to manufacturer's instructions, with 5′L-VH mix and 3′CγCH1 or 3′CαCH1 primers (Wardemann and Kofer, 2013), with the following PCR cycles: 2 min at 94°C, 50× (94°C for 30 s, 58°C for 30 s, and 72°C for 1 min), and 72°C for 5 min. PCR products were gel-purified using the NucleoSpin Clean-up kit (Macherey Nagel), and subjected to an additional PCR amplification (5 µl of template) following the aforementioned conditions but with 5′L-VH mix (for 7-155 and 7-176) or 5′L-VH3-30 (for 7-107/7-269) and 3′IgGint or 3′CαCH1-2 primers (Wardemann and Kofer, 2013), with a final in-gel purification step using the NucleoSpin Clean-up kit.

DNA quantification and DNA library preparation and sequencing were performed at the Biomics platform (Institut Pasteur) using Illumina technology. Briefly, DNA libraries were quantified and quality-checked using 5200 Fragment Analyzer System (Agilent Technologies) and then prepared using NEXTflex PCR-Free DNA Sequencing Kit (Bio Scientific) according to manufacturer's instructions (no fragmentation step). DNA fragments were loaded on the flow cell (20% Phix at 12.5 pM and 80% of library pool at 6 pM [vol/vol]) and sequenced using MiSeq Reagent Kit v3 (Illumina) and Miseq instrument, which generated 2× 300-bp paired-end reads. Forward and reverse reads with 10 overlapping nucleotides minimum were merged using PEAR software (Zhang et al., 2013) with the following parameters: minimum length, n = 300; quality threshold, q = 20; and minimum length after trimming low-quality parts, t = 300. Once merged, sequences were assigned with GL Ig genes using IgBlast (https://www.ncbi.nlm.nih.gov/igblast/), which was also used to remove sequences with low-quality features (stop codon, V-gene E-value >10^{-3}, undefined CDR_H3 and FWRs, or subject alignment starts >9) and database building. CD-HIT clustering program (http://weizhongli-lab.org/cd-hit/) allowed exclusion of redundant reads (99% identity), and only representative and isotype-checked sequences were then used to perform divergence/identity analyses using Needle program (http://embossgui.sourceforge.net/demo/manual/needle.html) to align and compute similarity scores with library sequences trimmed at the end of FWR3 and FWR4 for alignment with V-gene GL and pt7 bNAb reference sequence, respectively (gapopen, 10; gapextent, 0.5). Divergence/identity plots were generated using FlowJo (v10.7.1) after transforming for all final sequences in a given library (x, y) coordinates–containing text file into a FCS format file using DISCit software (Moreau and Bousso, 2014).

ELISAs

ELISAs were performed as previously described (Mouquet et al., 2011; Mouquet et al., 2012). Briefly, high-binding 96-well ELISA plates (Costar, Corning) were coated overnight with purified Env proteins (125 ng/well in PBS). After washing with 0.05% Tween 20-PBS (PBST), plates were blocked for 2 h with 2% bovine serum albumin and 1 mM EDTA-PBST (blocking solution), washed, and incubated with serially diluted purified serum IgG and recombinant monoclonal antibodies in PBS. For competition ELISAs, BG505 SOSIP.664 protein-coated plates were blocked, washed, and incubated for 2 h with biotinylated antibodies (at a concentration of 0.33, 3.33, or 6.67 nM) in 1:2 serially diluted solutions of antibody competitors in PBS (IgG concentration starting at 666.7 nM). After washing, plates were revealed by addition of goat HRP-conjugated anti-human IgG (Immunology Jackson ImmunoResearch) or HRP-conjugated streptavidin (BD Pharmingen; 0.8 µg/ml final in blocking solution) and HRP chromogenic substrate (ABTS solution; Euromedex). Binding of antibodies to overlapping linear peptides was tested using the same procedure as previously described (Mouquet et al., 2011; Mouquet et al., 2012). Experiments were performed using HydroSpeed microplate washer and Sunrise microplate absorbance reader (Tecan Männedorf), with optical density measurements made at 405 nm (OD_{405nm}). All antibodies were tested in duplicate or triplicate in at least two independent experiments, which included mGO53 negative and appropriate positive controls.

Protein microarrays

All experiments were performed at 4°C using ProtoArray Human Protein Microarrays (Thermo Fisher Scientific). Microarrays were blocked for 1 h in blocking solution (Thermo Fisher Scientific), washed, and incubated for 1 h 30 min with IgG antibodies at 2.5 µg/ml as previously described (Planchais et al., 2019). After washing, arrays were incubated for 1 h 30 min with AF647-conjugated goat anti-human IgG antibodies (at 1 µg/ml in PBS; Thermo Fisher Scientific) and revealed using GenePix 4000B microarray scanner (Molecular Devices) and GenePix Pro 6.0 software (Molecular Devices) as previously described (Planchais et al., 2019). Fluorescence intensities were quantified using Spotxel software (SICASYS Software), and mean fluorescence intensity (MFI) signals for each antibody (from duplicate protein spots) were plotted against the reference antibody mGO53 (nonpolyreactive isotype control) using Prism software (v8.1.2; GraphPad). For each antibody, Z-scores were calculated using ProtoArray Prospector software (v5.2.3; Thermo Fisher Scientific), and deviation (σ) to the diagonal and polyreactivity index (PI) values were calculated as previously described (Planchais et al., 2019). Antibodies were defined as polyreactive when PI > 0.21.

HEp-2 cell IFA

Binding of human anti-HIV-1 Env and control monoclonal IgG antibodies (mGO53 [Wardemann et al., 2003] and ED38 [Meffre et al., 2004]) to HEp-2 cell–expressing autoantigens was analyzed at 100 µg/ml by indirect IFA (ANA HEp-2 AeskuSlides; Aesku.Diagnostics) following the manufacturer's instructions in two independent experiments. IFA sections were examined using the fluorescence microscope Axio Imager 2 (Zeiss), and pictures were taken at magnification 40× with 5,000 ms–acquisition using ZEN imaging software (Zen 2.0 blue version; Zeiss) at the Photonic BioImaging platform (Institut Pasteur).

In vitro viral transcytosis assay

Transcytosis assays were performed using human epithelial HEC-1A cells (HTB-112; ATCC) cultivated on 0.4-µm polyethylene terephthalate Transwell membranes (Millicell; Millipore) and monitored for the formation of tight monolayers as described previously (Lorin et al., 2017). HIV-1 viruses (10 ng of p24) were incubated vol/vol for 1 h at 37°C with purified antibodies (66.67 nM final concentration), and mixtures were added onto epithelial cell monolayers at day 6 of culture. As controls, HIV-1 alone was added into inserts with cells (no Ab) and without cells (control), which takes into account the proportion of virions not passing through the Transwell filter. After 24 h, basal media were collected, and their p24 content was measured by ELISA (HIV-1 p24 Antigen Capture Assay; Advanced Bioscience Laboratories). The percentage of transcytosis was determined using the following formula: (concentration p24 sample/mean concentration p24 control) × 100. The infectivity of virions transcytosed in the presence or not of antibodies (0.05 ng p24) was measured using a previously described TZM-bl cells assay (Lorin et al., 2017). Two independent experiments were performed with triplicate Transwells and included non–HIV-1 isotype IgA control mGO53.

HIV-1 in vitro neutralization assay

Pseudoviruses (BaL.26, 6535.3, YU2.DG, RHPA4259.7, SC422661.8, CAAN5342.A2, and PVO.4; Env plasmids obtained from the NIH AIDS reagent program) were prepared by cotransfection of HEK-293T cells with pSG3ΔEnv vector using FUGENE-6 transfection reagent (Promega) as previously described (Li et al., 2005; Sarzotti-Kelsoe et al., 2014). High-mannose-only YU2 pseudoviruses were produced in HEK-293T cells treated with 25 µM kifunensine (Sigma-Aldrich). Pseudovirus-containing culture supernatants were harvested 2 d after transfection, and the 50% tissue culture infectious dose ($TCID_{50}$) of each preparation was determined using TZM-bl cells (NIH AIDS Reagent Program) as previously described (Li et al., 2005; Sarzotti-Kelsoe et al., 2014). Neutralization experiments were performed twice and included 10-1074 IgG or IgA as a positive control. Neutralization of HIV-1 strains in the cross-clade reference and extended virus panels (deCamp et al., 2013; Scheid et al., 2011) was measured using TZM-bl cells as previously described (Li et al., 2005). IC_{50} values were calculated using Prism software (v6.0a) by fitting duplicate values using the five-parameter sigmoidal dose–response model. Neutralizing activities of 7-269 IgA bNAb against clade B viruses from various infection periods (Bouvin-Pley et al., 2014) was assessed in duplicate using TZM-bl reporter cells. Viruses (400 $TCID_{50}$) were incubated for 1 h at 37°C with threefold serially diluted 7-269 IgA. The virus-IgA mixtures were then used to infect 10,000 TZM-bl cells in the presence of 37.5 µg/ml DEAE-dextran. Infection levels were determined after 48 h by measuring the luciferase activities of cell lysates as described previously (Bouvin-Pley et al., 2014).

ADCP assay

Biotinylated purified YU2 gp140-F proteins were incubated for 1 h at room temperature with 1 µm NeutrAvidin FITC-labeled microspheres (Invitrogen, Thermo Fisher Scientific; 1.2 µg for 3 µl of microspheres). Conjugated beads were then washed in 2% bovine serum albumin–PBS and diluted 1:10 in PBS. Purified IgG or IgA monoclonal antibodies (1.25 µg/ml final concentration) were mixed with gp140-F–conjugated beads (1:2,500 final dilution) and incubated 1 h at 37°C under gentle agitation. Mixtures were then incubated with 1.8×10^5 purified monocytes for 2 h at 37°C under gentle agitation. Cells were washed with PBS and fixed with 1% paraformadehyde-PBS. Data were acquired using a BD LSR Fortessa cytometer (BD) and analyzed using FlowJo software (v10.7.1). Phagocytic scores (PSs) were calculated as previously described (Tay et al., 2016): a cutoff was first assigned based on the 95th percentile of the no-antibody control (no Ab). For each sample, the PS was calculated as follows: (% FITC subset 95th Ab × MFI FITC subset 95th Ab)/(% FITC subset 95th no Ab × MFI FITC subset 95th no Ab). PSs were then normalized by the PS of mGO53 isotype control.

Flow cytometric antibody binding to infected cells

Laboratory-adapted (AD8 and YU2) and T/F (CH058, CH077, and THRO) viruses were produced from infectious molecular clones (NIH AIDS Reagent Program) as previously described (Bruel et al., 2016; Bruel et al., 2017). CEM.NKR-CCR5 cells (NIH AIDS Reagent Program) were infected with inocula of selected viruses and adjusted to achieve 10–40% of Gag^+ cells 48 h after infection (Bruel et al., 2016; Bruel et al., 2017). Infected cells were incubated with IgG and IgA antibodies (at 15 µg/ml) in staining buffer (PBS, 0.5% bovine serum albumin, and 2 mM EDTA) for 30 min at 37°C, washed, and incubated for 30 min at 4°C with AF647-conjugated anti-human IgG antibodies (1:400 dilution; Life Technologies) or with mouse anti-human IgA HB200 antibodies (30 µg/ml final; Lorin and Mouquet, 2015) for 30 min and 1 h, respectively, at 4°C. Binding reactions using HB200 were revealed after washing using 1:400-diluted Alexa Fluor 647–conjugated goat anti-mouse antibodies (Thermo Fisher Scientific) for 30 min at 4°C. Cells were then fixed with 4% paraformaldehyde and stained for intracellular Gag as previously described (Bruel et al., 2016; Bruel et al., 2017). Data were acquired using an Attune Nxt instrument (Life Technologies, Thermo Fisher Scientific) and analyzed using FlowJo software (v10.7.1).

NK-based ADCC assay

The ADCC assay was performed as previously described (Bruel et al., 2016). Briefly, AD8-infected CEM.NKR-CCR5 cells were stained with CellTrace Far Red cell proliferation kit (Thermo Fisher Scientific) for 30 min at 37°C and incubated with antibodies for 5 min at room temperature in U-bottom 96-well plates (2×10^4 target cells with antibodies at 15 µg/ml final concentration). For the ADCC competition assay, the target cells were incubated with anti-gp120 IgG antibodies in the presence of 7-269 IgAs (both at 15 µg/ml final concentration). 2×10^5 purified human NK cells were then added (1 CEM.NKR:10 NK) and incubated for 4 h at 37°C, following a brief spindown to promote cell contacts. Cells were then stained for intracellular Gag as previously described (Bruel et al., 2016), and LIVE-DEAD fixable aqua dead cell marker (1:1,000 in PBS; Life Technologies, Thermo Fisher Scientific) was added for 20 min at 4°C before

fixation. Data were acquired using an Attune Nxt instrument (Life Technologies, Thermo Fisher Scientific) and analyzed using FlowJo software (v10.7.1). The frequencies of Gag^+ cells among $Far\text{-}Red^+$ cells were determined. The percentage of ADCC was calculated using the following formula: 100 × (% of Gag^+ target cells plus NK without antibody − % of Gag^+ target cells plus effector with antibody)/(% of Gag^+ target cells plus NK without antibody).

Monocyte- and neutrophil-based ADCC assays

AD8-infected CEM.NKR-CCR5 cells were first stained using the CellTrace Far Red cell proliferation kit (Invitrogen, Thermo Fisher Scientific) for 30 min at 37°C. 4×10^4 target cells were then incubated for 5 min at room temperature with antibodies (at 15 µg/ml final concentration) and mixed 1:1 with 2, 4, or 8×10^5 human monocytes and neutrophils. Following a brief spindown to promote cell contacts, mixtures were incubated for 4 h at 37°C. Cells were fixed and stained for intracellular Gag using KC57-RD1 antibody (diluted 1:500; Beckman Coulter). Data were acquired using an Attune Nxt instrument (Life Technologies, Thermo Fisher Scientific) and analyzed using FlowJo software (v10.7.1).

HIV-1–infected hu-mice

Animal experiments were approved by a local institutional ethical committee (Institut Pasteur) and validated by the French Ministry of Education and Research (MENESR #02162.01). BRGS mice, housed in micro-isolators under pathogen-free conditions, were used as recipients to create hu-mice as previously described (Li et al., 2018; Masse-Ranson et al., 2019). Briefly, newborn pups (3–5 d old) received sublethal irradiation (3 Gy) and were injected intrahepatically with 5–10 × 10^4 $CD34^+CD38^-$ human fetal liver cells. HIV infection was performed with 15–20-wk-old mice. NLAD8 viruses were produced by transfection of HEK-293T cells with pNLAD8 plasmid (HIV-1 NLAD8 molecular clone; NIH AIDS Reagent Program) and titrated on activated PBMCs by the Reed–Muench method using the Alliance HIV-1 p24 ELISA kit (PerkinElmer). Hu-mice were inoculated using i.p. injection of 10^5 $TCID_{50}$ HIV_{NLAD8}. Viral RNA was extracted from plasma (25 µl) using QIAamp Viral RNA kit (Qiagen), and plasma viremia was assayed using Retro-transcription (RNA Invitrogen) and linear 15-cycle pre-amplification PCR, followed by probe-based quantitative PCR (JumpStart; Sigma-Aldrich) using previously described primers, probes, and standards (Li et al., 2018; Masse-Ranson et al., 2019). ART in infected mice (oral administration of a three-drug regimen: 72.9 mg/kg Emtricitabine [FTC, Emtriva; Gilead], 72.9 mg/kg Tenofovir disporxyl fumarate [Viread; Gilead], and 729.17 mg/kg Raltegravir [Isentress, MSD] per day in the water gel delivery system) was initiated at 12 dpi for 3–4 wk. 7-269 and mGO53 isotype control were administrated i.p. as a single dose of endotoxin-free purified IgA (0.5 mg) during ART regimen, which was stopped 1 d after the antibody injection. FACS analysis on total blood was performed as previously described (Li et al., 2018; Masse-Ranson et al., 2019).

Sample preparation and cryo-EM

IgA Fab-expression vector was generated from the original IgG1-expression vector (Tiller et al., 2008) by substituting the entire DNA sequence coding the IgG1 constant region by one stopping at end of the IgA1-C_H1 domain, followed by a hexa-Histidine (6xHis)-Tag (synthetic DNA fragments, GeneArt; Thermo Fisher Scientific). 7-269 IgH was cloned into the IgA1-Fab, and 7-155, 7-176, 3BNC117, and 35O22 (Huang et al., 2014) IgH into the IgG1-Fab (Mouquet et al., 2012) expression vectors. Recombinant Fab fragments were produced by transient cotransfection of Freestyle 293-F suspension cells (Thermo Fisher Scientific) and purified using Ni-Sepharose Excel affinity chromatography as described above. Purified protein fractions were dialyzed against DPBS (Gibco). A codon-optimized DNA fragment coding for soluble BG505 SOSIP.664 without C-terminal tags but preceded by the t-PA signal peptide was synthesized (Genscript) and cloned into pcDNA3.1/Zeo$^{(+)}$ expression vector (Thermo Fisher Scientific). BG505 SOSIP.664 was produced by transfecting Freestyle 293-F cells and purified using PGT145-based affinity chromatography as described above. Proteins were eluted using 3 M $MgCl_2$, and buffer was immediately exchanged into SEC buffer (10 mM Tris and 75 mM NaCl, pH 8), followed by SEC purification on a Superose 6 10/300 column (GE Healthcare). Peak fractions corresponding to SOSIP trimers were pooled and concentrated for immediate use or storage at −80°C.

Complexes were prepared by incubating purified BG505 SOSIP.664 overnight at 4°C with the corresponding Fabs at a 3:1 Fab/gp120 protomer molar ratio. SOSIP-7-269-3BNC117 and SOSIP-7-176 complexes were further separated by SEC on a Superose 6 10/300 column, and fractions containing Env-Fab complexes were pooled, concentrated, and used for sample preparation. 3 µl of diluted complexes (0.6 µM final concentration in SEC buffer) were added to C-flat R2/2 300 mesh copper grids (Electron Microscopy Sciences), which were glow-discharged beforehand using an ELMO glow discharge system at 2 mA for 30 s (Cordouan Technologies). Samples were immediately vitrified in 100% liquid ethane using a Mark IV Vitrobot (Thermo Fisher Scientific) by blotting for 4 s with Whatman No. 1 filter paper at 9°C and 100% relative humidity, after 30-s waiting time. The complex SOSIP-7-155 was not purified by SEC; instead, the sample was diluted to 0.45 µM after overnight binding incubation and used for grid preparation as indicated for the other samples.

Cryo-EM data collection, refinement, and modeling

Single-particle cryo-EM data of the SOSIP-7-269-3BNC117 complex were acquired on a Titan Krios transmission electron microscope (Thermo Fisher Scientific) operating at 300 kV, using EPU automated image acquisition software (Thermo Fisher Scientific). Videos were collected on a Gatan K3 direct electron detector operating in Counted Super Resolution mode at a nominal magnification of 105,000× (0.85 Å/pixel) using a defocus range of −1.0 to −3.0 µm. Movies were collected over a 3-s exposure and a total dose of ∼45 e−/Å^2. Data for the SOSIP-7-155 and SOSIP-7-176 complexes were collected on a Glacios electron microscope (Thermo Fisher Scientific) operated at 200 kV and equipped with a Falcon 3EC direct electron detector. Movies were collected in linear mode using a pixel size of 2.0 Å. The defocus range was −1.0 to −3.0 µm, and each movie contained 38 frames with a dose of ∼60 e−/Å^2 and a 1.67-s exposure time.

Data were processed by using Relion-3.0 (Nakane et al., 2018), running on a Linux workstation equipped with four GPUs following the workflow shown in Data S1 and Data S2. In brief, row movies were processed using MotionCor2 (Zheng et al., 2017), with a five-by-five patch-based alignment, keeping all frame and dose-weighting up to the total exposure. The contrast transfer functions (CTFs) of the dose-weighted images were determined using CTFfind-4.1 (Rohou and Grigorieff, 2015). The images having a CTF maximal resolution worse than 4 Å (Titan Krios images) or 7–8 Å (Glacios images) were discarded. Images were then manually inspected, and those presenting important ice contamination or large carbon area were also removed. Particles were picked using the Relion Laplacian of Gaussian with filter minimum and maximum diameters of 100 and 200 Å. They were extracted in boxes of 360 × 360 Å^2 (SOSIP-7-269-3BNC117) and 440 × 440 Å^2 (SOSIP-7-155; SOSIP-7-176) and submitted to several rounds of 2D classifications until only suitable classes (with well-defined features and no Einstein-from-the-noise aspect) remained. The strategy was then adapted with respect to the number of remaining particles and the ability to obtain a correct preliminary model. In the case of the SOSIP-7-176 complex, a small number of representative 2D classes were used to perform a new particle picking with 2D references. Particles were submitted to rounds of 2D classification and to an extensive 3D classification without symmetry. Those belonging to the best 3D class were used to build a refined map with C3 symmetry at 7-Å resolution. In the case of the SOSIP-7-155 complex, an initial 3D map was built and refined at 6.7-Å resolution. This map (filtered at 1.5 nm) was used to perform a new particle picking with 3D reference. Particles were submitted to rounds of 2D classification and to an extensive 3D classification without symmetry. Those belonging to the best 3D class were used to build a new refined map with C3 symmetry at 6.3-Å resolution. Finally, for the SOSIP-7-269-3BNC117 complex, a second round of particle picking was not necessary. Particles from the 2D classification rounds were submitted to a 3D classification, and those belonging to the best 3D class were used to build a first refined map at 3.4-Å resolution. This map was used to perform per-particle CTF refinement, particle polishing, and another per-particle CTF refinement (shiny particles). A new map was refined at 2.9-Å resolution, but its quality was heterogeneous (the Fab variable region was well defined but not the heavy chain), so the shiny particles were transferred to cryoSPARC-v2 (Punjani et al., 2017), and a new map was built using nonuniform refinement procedure (Punjani et al., 2020), which resulted in a slight increase of the quality but did not completely solve the problem. In parallel, the shiny particles were also submitted to an extensive 3D classification in Relion. Those belonging to the best class were submitted to a C3 symmetry particle expansion and to a new 3D extensive classification using a local mask encompassing one of the HIV Env protomers and one 7-269 Fab. Particles belonging to the most populated 3D class were finally used to perform a 3D refinement in the local mask, resulting in a 3.0-Å resolution map in which both chains of the Fab variable region were well defined.

A model for the V_H and V_L domains of 7-269 obtained from the Phyre2 server (Kelley et al., 2015) was fitted into the locally refined cryo-EM density map using UCSF Chimera (Pettersen et al., 2004). This initial model was refined into the map using one round of rigid body morphing and simulated annealing in Phenix (Liebschner et al., 2019), followed by iterative rounds of manual building and real-space and B-factor refinement in Coot (Emsley et al., 2010) and Phenix (Liebschner et al., 2019), with secondary structure restraints. The 7-269 variable region structure was then used, along with the SOSIP-3BNC117 structure (PDB accession no. 5V8M), as initial coordinates that were fitted into the EM map of the trimeric complex (nonuniform refinement) using UCSF Chimera (Pettersen et al., 2004). As mentioned above, a first round of refinement using rigid body morphing and simulated annealing in Phenix (Liebschner et al., 2019) was followed by manual building and iterative rounds of real-space and B-factor refinement in Coot (Emsley et al., 2010) and Phenix (Liebschner et al., 2019). Modeling of glycans was performed by interpreting cryo-EM density at PNGS in Coot (Emsley et al., 2010). Validation of model coordinates was performed using MolProbity (Williams et al., 2018).

Statistics

Groups of mice treated with 7-269 and control IgA antibodies were compared by Kaplan–Meier analysis for viral rebound using log-rank (Mantel–Cox) test. Percentages of transcytosis and post-transcytosis infectivity levels were compared for each bNAb group to the no antibody (no Ab) control using Mann–Whitney test. ADCC percentages were compared between groups (in the presence or not of IgA competitor) using two-tailed Wilcoxon test. ADCP activities (nPS and % Gag$^+$ cells) were compared between groups using two-tailed Mann–Whitney test. Statistical analyses were performed using Prism software (v8.1.2).

Online supplemental material

Fig. S1 shows the HIV-1–neutralizing activity of pt7-derived IgG and IgA serum and monoclonal antibodies. Fig. S2 presents the IgA profiles of pt7 bNAbs and purified serum antibodies. Fig. S3 shows the lineage tracing by high-throughput immunoglobulin sequencing of pt7 bNAbs in the blood and bone marrow samples. Fig. S4 shows the expression of Fc receptors on human immune effector cells used in the ADCC and ADCP assays. Fig. S5 shows the interactions at the BG505 SOSIP-7-269 Fab interface. Table S1 provides details on the immunoglobulin gene repertoire and reactivity of Env-captured human memory B cell antibodies from pt7. Table S2 shows the human proteoarray hits for 7-176 antibody cross-reactivity to human proteins. Table S3 presents the cryo-EM data collection, refinement, and validation statistics for BG505 SOSIP-7-269 Fab complexes. Table S4 provides the buried surface area of 7-269 for each gp120 glycan. Table S5 provides the buried surface area of gp120 for 7-269 Fab IgH and IgL. Data S1 and Data S2 show the cryo-EM data collection and processing of the SOSIP-7-269-3BNC117, SOSIP-7-155, and SOSIP-7-176 complexes.

Data availability

Density maps and atomic coordinates for the BG505 SOSIP.664-7-269-3BNC117 complex were deposited in the Electron

Microscopy Data Bank and Protein Data Bank with accession numbers EMD-13316 and PDB 7PC2. The density maps for the BG505 SOSIP.664-7-176 and -7-155 complexes were deposited with the numbers EMD-13332 and EMD-13333, respectively.

Acknowledgments

We are grateful to all participants who consented to be part of this study. We thank Arlene M. Hurley (the Rockefeller University Hospital) and Nathalie Jolly from the clinical core of the Center for Translational Sciences (Institut Pasteur) for their assistance on the preparation of the BHUANTIVIH protocol, Sandrine Schmutz and Sophie Novault (Unité de Technologie et Service - Cytométrie et Biomarqueurs, Institut Pasteur) for their help with single-cell sorting, and Laurence Ma (Biomics Platform, Institut Pasteur) for Illumina sequencing. We thank Natalia T. Freund (Tel Aviv University) for kindly providing BG8/BG18 expression vectors and Rogier W. Sanders (University of Amsterdam) and John P. Moore (Weill Medical College of Cornell University) for kindly providing BG505 SOSIP.664 expression vectors. We also thank the Core Facility Cryo-electron Microscopy and Tomography of Central European Institute of Technology Masaryk University for the initial support to the project, and the NanoImaging Core at Institut Pasteur for support with sample preparation and image acquisition of the data presented in this paper.

The NanoImaging Core was created with the help of a grant from the French Government's Investissements d'Avenir program (EQUIPEX CACSICE - Centre d'analyse de systèmes complexes dans les environnements complexes, ANR-11-EQPX-0008). We thank the NIH AIDS Reagent Program (Division of AIDS, National Institute of Allergy and Infectious Diseases, NIH) for contributing to reagents and the Agence National de Recherche sur le SIDA et les hépatites virales (ANRS) for an equipment grant support. The Biomics platform is supported by France Génomique (ANR-10-INBS-09-09) and IBISA. I. Fernández and C. Planchais were recipients of an ANRS postdoctoral fellowship. The J.P. Di Santo laboratory received support from the Vaccine Research Institute (Créteil, France). H. Mouquet received core grants from the Institut Pasteur, Institut national de la santé et de la recherche médicale, and the Milieu Intérieur Program (ANR-10-LABX-69-01). This work was supported by the European Research Council Seventh Framework Program (ERC-2013-StG 337146), and by Gilead Sciences HIV Cure Grants (#00397).

Author contributions: H. Mouquet conceived and supervised the study. M. Braibant, M.S. Seaman, J.P. Di Santo, F.A. Rey, and H. Mouquet supervised the experiments. V. Lorin, I. Fernández, G. Masse-Ranson, M. Bouvin-Pley, G. Girelli-Zubani, C. Planchais, O. Fiquet, J.D. Dimitrov, and H. Mouquet designed, performed, and analyzed the experiments. I. Fernández, G. Péhau-Arnaudet, D. Hrebík, and P. Plevka collected and I. Fernández, F. Bontems processed the cryo-EM data. T. Hieu carried out bioinformatics analyses. B.D. Walker, and J.F. Scheid provided human samples and personal data. L.M. Molinos-Albert, F. Guivel-Benhassine, R.W. Sanders, and O. Schwartz contributed with key reagents and expertise. V. Lorin and H. Mouquet wrote the manuscript with contributions from all the authors.

Disclosures: F.A. Rey is a board member of EureKARE and MELETIUS Therapeutics. No other disclosures were reported.

Submitted: 1 October 2021
Revised: 3 January 2022
Accepted: 12 January 2022

References

Anthony, C., T. York, V. Bekker, D. Matten, P. Selhorst, R.C. Ferreria, N.J. Garrett, S.S.A. Karim, L. Morris, N.T. Wood, et al. 2017. Cooperation between strain-specific and broadly neutralizing responses limited viral escape and prolonged the exposure of the broadly neutralizing epitope. *J. Virol.* 91:e00828-17. https://doi.org/10.1128/jvi.00828-17

Astronomo, R.D., S. Santra, L. Ballweber-Fleming, K.G. Westerberg, L. Mach, T. Hensley-McBain, L. Sutherland, B. Mildenberg, G. Morton, N.L. Yates, et al. 2016. Neutralization takes precedence over IgG or IgA isotype-related functions in mucosal HIV-1 antibody-mediated protection. *EBioMed.* 14:97–111. https://doi.org/10.1016/j.ebiom.2016.11.024

Barnes, C.O., H.B. Gristick, N.T. Freund, A. Escolano, A.Y. Lyubimov, H. Hartweger, A.P. West, A.E. Cohen, M.C. Nussenzweig, and P.J. Bjorkman. 2018. Structural characterization of a highly-potent V3-glycan broadly neutralizing antibody bound to natively-glycosylated HIV-1 envelope. *Nat. Comm.* 9:1251. https://doi.org/10.1038/s41467-018-03632-y

Behrens, A.J., S. Vasiljevic, L.K. Pritchard, D.J. Harvey, R.S. Andev, S.A. Krumm, W.B. Struwe, A. Cupo, A. Kumar, N. Zitzmann, et al. 2016. Composition and antigenic effects of individual glycan sites of a trimeric HIV-1 envelope glycoprotein. *Cell Rep.* 14:2695–2706. https://doi.org/10.1016/j.celrep.2016.02.058

Black, K.P., J.E. Cummins Jr., and S. Jackson. 1996. Serum and secretory IgA from HIV-infected individuals mediate antibody-dependent cellular cytotoxicity. *Clin. Immunol. Immunopathol.* 81:182–190. https://doi.org/10.1006/clin.1996.0175

Bonsignori, M., E.F. Kreider, D. Fera, R.R. Meyerhoff, T. Bradley, K. Wiehe, S.M. Alam, B. Aussedat, W.E. Walkowicz, K.K. Hwang, et al. 2017. Staged induction of HIV-1 glycan-dependent broadly neutralizing antibodies. *Sci. Transl. Med.* 9:eaai7514. https://doi.org/10.1126/scitranslmed.aai7514

Bournazos, S., F. Klein, J. Pietzsch, M.S. Seaman, M.C. Nussenzweig, and J.V. Ravetch. 2014. Broadly neutralizing anti-HIV-1 antibodies require Fc effector functions for in vivo activity. *Cell*. 158:1243–1253. https://doi.org/10.1016/j.cell.2014.08.023

Bouvin-Pley, M., M. Morgand, L. Meyer, C. Goujard, A. Moreau, H. Mouquet, M. Nussenzweig, C. Pace, D. Ho, P.J. Bjorkman, et al. 2014. Drift of the HIV-1 envelope glycoprotein gp120 toward increased neutralization resistance over the course of the epidemic: a comprehensive study using the most potent and broadly neutralizing monoclonal antibodies. *J. Virol.* 88:13910–13917. https://doi.org/10.1128/JVI.02083-14

Bruel, T., F. Guivel-Benhassine, S. Amraoui, M. Malbec, L. Richard, K. Bourdic, D.A. Donahue, V. Lorin, N. Casartelli, N. Noel, et al. 2016. Elimination of HIV-1-infected cells by broadly neutralizing antibodies. *Nat. Commun.* 7:10844. https://doi.org/10.1038/ncomms10844

Bruel, T., F. Guivel-Benhassine, V. Lorin, H. Lortat-Jacob, F. Baleux, K. Bourdic, N. Noel, O. Lambotte, H. Mouquet, and O. Schwartz. 2017. Lack of ADCC breadth of human nonneutralizing anti-HIV-1 antibodies. *J. Virol.* 91:e02440-16. https://doi.org/10.1128/JVI.02440-16

Calarese, D.A., C.N. Scanlan, M.B. Zwick, S. Deechongkit, Y. Mimura, R. Kunert, P. Zhu, M.R. Wormald, R.L. Stanfield, K.H. Roux, et al. 2003. Antibody domain exchange is an immunological solution to carbohydrate cluster recognition. *Science*. 300:2065–2071. https://doi.org/10.1126/science.1083182

Caskey, M., F. Klein, and M.C. Nussenzweig. 2019. Broadly neutralizing anti-HIV-1 monoclonal antibodies in the clinic. *Nat. Med.* 25:547–553. https://doi.org/10.1038/s41591-019-0412-8

Cheeseman, H.M., A.M. Carias, A.B. Evans, N.J. Olejniczak, P. Ziprin, D.F. King, T.J. Hope, and R.J. Shattock. 2016. Expression profile of human Fc receptors in mucosal tissue: Implications for antibody-dependent cellular effector functions targeting HIV-1 transmission. *PLoS One*. 11:e0154656. https://doi.org/10.1371/journal.pone.0154656

Cheeseman, H.M., N.J. Olejniczak, P.M. Rogers, A.B. Evans, D.F.L. King, P. Ziprin, H.X. Liao, B.F. Haynes, and R.J. Shattock. 2017. Broadly

neutralizing antibodies display potential for prevention of HIV-1 infection of mucosal tissue superior to that of nonneutralizing antibodies. *J. Virol.* 91:e01762-16. https://doi.org/10.1128/JVI.01762-16

Daniels, C.N., and K.O. Saunders. 2019. Antibody responses to the HIV-1 envelope high mannose patch. *Adv. Immunol.* 143:11–73. https://doi.org/10.1016/bs.ai.2019.08.002

deCamp, A., P. Hraber, R.T. Bailer, M.S. Seaman, C. Ochsenbauer, J. Kappes, R. Gottardo, P. Edlefsen, S. Self, H. Tang, et al. 2013. Global panel of HIV-1 env reference strains for standardized assessments of vaccine-elicited neutralizing antibodies. *J. Virol.* 88:2489–2507. https://doi.org/10.1128/JVI.02853-13

Doria-Rose, N.A., and E. Landais. 2019. Coevolution of HIV-1 and broadly neutralizing antibodies. *Curr. Opin HIV AIDS*. 14:286–293. https://doi.org/10.1097/COH.0000000000000550

Doria-Rose, N.A., C.A. Schramm, J. Gorman, P.L. Moore, J.N. Bhiman, B.J. DeKosky, M.J. Ernandes, I.S. Georgiev, H.J. Kim, M. Pancera, et al. 2014. Developmental pathway for potent V1V2-directed HIV-neutralizing antibodies. *Nature*. 509:55–62. https://doi.org/10.1038/nature13036

Duchemin, M., M. Khamassi, L. Xu, D. Tudor, and M. Bomsel. 2018. IgA targeting human immunodeficiency virus-1 envelope gp41 triggers antibody-dependent cellular cytotoxicity cross-clade and cooperates with gp41-specific IgG to increase cell lysis. *Front Immunol.* 9:244. https://doi.org/10.3389/fimmu.2018.00244

Duchemin, M., D. Tudor, A. Cottignies-Calamarte, and M. Bomsel. 2020. Antibody-dependent cellular phagocytosis of HIV-1-Infected cells is efficiently triggered by IgA targeting HIV-1 envelope subunit gp41. *Front Immunol.* 11:1141. https://doi.org/10.3389/fimmu.2020.01141

Emsley, P., B. Lohkamp, W.G. Scott, and K. Cowtan. 2010. Features and development of Coot. *Acta Crystallogr. D Biol. Crystallogr.* 66:486–501. https://doi.org/10.1107/S0907444910007493

Fischinger, S., S. Dolatshahi, M.F. Jennewein, S. Rerks-Ngarm, P. Pitisuttithum, S. Nitayaphan, N. Michael, S. Vasan, M.E. Ackerman, H. Streeck, and G. Alter. 2020. IgG3 collaborates with IgG1 and IgA to recruit effector function in RV144 vaccinees. *JCI Insight*. 5:e140925. https://doi.org/10.1172/jci.insight.140925

Freund, N.T., H. Wang, L. Scharf, L. Nogueira, J.A. Horwitz, Y. Bar-On, J. Golijanin, S.A. Sievers, D. Sok, H. Cai, et al. 2017. Coexistence of potent HIV-1 broadly neutralizing antibodies and antibody-sensitive viruses in a viremic controller. *Sci. Transl. Med.* 9:eaal2144. https://doi.org/10.1126/scitranslmed.aal2144

Gao, F., M. Bonsignori, H.X. Liao, A. Kumar, S.M. Xia, X. Lu, F. Cai, K.K. Hwang, H. Song, T. Zhou, et al. 2014. Cooperation of B cell lineages in induction of HIV-1-broadly neutralizing antibodies. *Cell*. 158:481–491. https://doi.org/10.1016/j.cell.2014.06.022

Garces, F., J.H. Lee, N. de Val, A.T. de la Pena, L. Kong, C. Puchades, Y. Hua, R.L. Stanfield, D.R. Burton, J.P. Moore, et al. 2015. Affinity maturation of a potent family of HIV antibodies is primarily focused on accommodating or avoiding glycans. *Immunity*. 43:1053–1063. https://doi.org/10.1016/j.immuni.2015.11.007

Gayet, R., E. Michaud, F. Nicoli, B. Chanut, M. Paul, N. Rochereau, C. Guillon, Z. He, L. Papagno, G. Bioley, et al. 2020. Impact of IgA isoforms on their ability to activate dendritic cells and to prime T cells. *Eur. J. Immunol.* 50:1295–1306. https://doi.org/10.1002/eji.201948177

Gray, E.S., M.A. Moody, C.K. Wibmer, X. Chen, D. Marshall, J. Amos, P.L. Moore, A. Foulger, J.S. Yu, B. Lambson, et al. 2011. Isolation of a monoclonal antibody that targets the alpha-2 helix of gp120 and represents the initial autologous neutralizing-antibody response in an HIV-1 subtype C-infected individual. *J. Virol.* 85:7719–7729. https://doi.org/10.1128/JVI.00563-11

Huang, J., B.H. Kang, M. Pancera, J.H. Lee, T. Tong, Y. Feng, H. Imamichi, I.S. Georgiev, G.Y. Chuang, A. Druz, et al. 2014. Broad and potent HIV-1 neutralization by a human antibody that binds the gp41-gp120 interface. *Nature*. 515:138–142. https://doi.org/10.1038/nature13601

Jia, M., R.A. Liberatore, Y. Guo, K.W. Chan, R. Pan, H. Lu, E. Waltari, E. Mittler, K. Chandran, A. Finzi, et al. 2020. VSV-displayed HIV-1 envelope identifies broadly neutralizing antibodies class-switched to IgG and IgA. *Cell Host Microbe*. 27:963–975.e5. https://doi.org/10.1016/j.chom.2020.03.024

Kelley, L.A., S. Mezulis, C.M. Yates, M.N. Wass, and M.J. Sternberg. 2015. The Phyre2 web portal for protein modeling, prediction and analysis. *Nat. Protoc.* 10:845–858. https://doi.org/10.1038/nprot.2015.053

Klein, F., C. Gaebler, H. Mouquet, D.N. Sather, C. Lehmann, J.F. Scheid, Z. Kraft, Y. Liu, J. Pietzsch, A. Hurley, et al. 2012. Broad neutralization by a combination of antibodies recognizing the CD4 binding site and a new conformational epitope on the HIV-1 envelope protein. *J. Exp. Med.* 209:1469–1479. https://doi.org/10.1084/jem.20120423

Klein, F., H. Mouquet, P. Dosenovic, J.F. Scheid, L. Scharf, and M.C. Nussenzweig. 2013. Antibodies in HIV-1 vaccine development and therapy. *Science*. 341:1199–1204. https://doi.org/10.1126/science.1241144

Kong, L., A. Torrents de la Peña, M.C. Deller, F. Garces, K. Sliepen, Y. Hua, R.L. Stanfield, R.W. Sanders, and I.A. Wilson. 2015a. Complete epitopes for vaccine design derived from a crystal structure of the broadly neutralizing antibodies PGT128 and 8ANC195 in complex with an HIV-1 Env trimer. *Acta Crystallogr. D Biol. Crystallogr.* 71:2099–2108. https://doi.org/10.1107/S1399004715013917

Kong, L., I.A. Wilson, and P.D. Kwong. 2015b. Crystal structure of a fully glycosylated HIV-1 gp120 core reveals a stabilizing role for the glycan at Asn262. *Proteins*. 83:590–596. https://doi.org/10.1002/prot.24747

Krebs, S.J., Y.D. Kwon, C.A. Schramm, W.H. Law, G. Donofrio, K.H. Zhou, S. Gift, V. Dussupt, I.S. Georgiev, S. Schatzle, et al. 2019. Longitudinal analysis reveals early development of three MPER-directed neutralizing antibody lineages from an HIV-1-Infected individual. *Immunity*. 50:677–691.e13. https://doi.org/10.1016/j.immuni.2019.02.008

Kumar, S., B. Ju, B. Shapero, X. Lin, L. Ren, L. Zhang, D. Li, Z. Zhou, Y. Feng, C. Sou, et al. 2020. A V_H1-69 antibody lineage from an infected Chinese donor potently neutralizes HIV-1 by targeting the V3 glycan supersite. *Sci. Adv*. 6:eabb1328. https://doi.org/10.1126/sciadv.abb1328

Kumar, S., H. Panda, M.A. Makhdoomi, N. Mishra, H.A. Safdari, H. Chawla, H. Aggarwal, E.S. Reddy, R. Lodha, S. Kumar Kabra, et al. 2019. An HIV-1 broadly neutralizing antibody from a clade C-infected pediatric elite neutralizer potently neutralizes the contemporaneous and autologous evolving viruses. *J. Virol.* 93:e01495-18. https://doi.org/10.1128/JVI.01495-18

Kwong, P.D., and J.R. Mascola. 2018. HIV-1 vaccines based on antibody identification, B cell ontogeny, and epitope structure. *Immunity*. 48:855–871. https://doi.org/10.1016/j.immuni.2018.04.029

Li, M., F. Gao, J.R. Mascola, L. Stamatatos, V.R. Polonis, M. Koutsoukos, G. Voss, P. Goepfert, P. Gilbert, K.M. Greene, et al. 2005. Human immunodeficiency virus type 1 env clones from acute and early subtype B infections for standardized assessments of vaccine-elicited neutralizing antibodies. *J. Virol.* 79:10108–10125. https://doi.org/10.1128/JVI.79.16.10108-10125.2005

Li, Y., G. Masse-Ranson, Z. Garcia, T. Bruel, A. Kok, H. Strick-Marchand, G. Jouvion, N. Serafini, A.I. Lim, M. Dusseaux, et al. 2018. A human immune system mouse model with robust lymph node development. *Nat. Methods*. 15:623–630. https://doi.org/10.1038/s41592-018-0071-6

Liebschner, D., P.V. Afonine, M.L. Baker, G. Bunkoczi, V.B. Chen, T.I. Croll, B. Hintze, L.W. Hung, S. Jain, A.J. McCoy, et al. 2019. Macromolecular structure determination using X-rays, neutrons and electrons: recent developments in Phenix. *Acta Crystallogr. D Struct. Biol.* 75:861–877. https://doi.org/10.1107/S2059798319011471

Longo, N.S., M.S. Sutton, A.R. Shiakolas, J. Guenaga, M.C. Jarosinski, I.S. Georgiev, K. McKee, R.T. Bailer, M.K. Louder, S. O'Dell, et al. 2016. Multiple antibody lineages in one donor target the glycan-V3 supersite of the HIV-1 envelope glycoprotein and display a preference for quaternary binding. *J. Virol.* 90:10574–10586. https://doi.org/10.1128/JVI.01012-16

Lopez, E., R.J. Shattock, S.J. Kent, and A.W. Chung. 2018. The multifaceted nature of immunoglobulin A and its complex role in HIV. *AIDS Res. Hum. Retroviruses*. 34:727–738. https://doi.org/10.1089/AID.2018.0099

Lorin, V., M. Malbec, C. Eden, T. Bruel, F. Porrot, M.S. Seaman, O. Schwartz, and H. Mouquet. 2017. Broadly neutralizing antibodies suppress post-transcytosis HIV-1 infectivity. *Mucosal Immunol.* 10:814–826. https://doi.org/10.1038/mi.2016.106

Lorin, V., and H. Mouquet. 2015. Efficient generation of human IgA monoclonal antibodies. *J. Immunol. Methods*. 422:102–110. https://doi.org/10.1016/j.jim.2015.04.010

Lu, C.L., D.K. Murakowski, S. Bournazos, T. Schoofs, D. Sarkar, A. Halper-Stromberg, J.A. Horwitz, L. Nogueira, J. Golijanin, A. Gazumyan, et al. 2016. Enhanced clearance of HIV-1-infected cells by broadly neutralizing antibodies against HIV-1 in vivo. *Science*. 352:1001–1004. https://doi.org/10.1126/science.aaf1279

MacLeod, D.T., N.M. Choi, B. Briney, F. Garces, L.S. Ver, E. Landais, B. Murrell, T. Wrin, W. Kilembe, C.H. Liang, et al. 2016. Early antibody lineage diversification and independent limb maturation lead to broad HIV-1 neutralization targeting the env high-mannose patch. *Immunity*. 44:1215–1226. https://doi.org/10.1016/j.immuni.2016.04.016

Magri, G., and A. Cerutti. 2020. IgA summons IgG to take a hit at HIV-1. *Cell Host Microbe*. 27:854–856. https://doi.org/10.1016/j.chom.2020.05.017

Masse-Ranson, G., M. Dusseaux, O. Fiquet, S. Darche, M. Boussand, Y. Li, S. Lopez-Lastra, N. Legrand, E. Corcuff, A. Toubert, et al. 2019. Accelerated

thymopoiesis and improved T-cell responses in HLA-A2/-DR2 transgenic BRGS-based human immune system mice. *Eur. J. Immunol.* 49: 954–965. https://doi.org/10.1002/eji.201848001

McCoy, L.E. 2018. The expanding array of HIV broadly neutralizing antibodies. *Retrovirology*. 15:70. https://doi.org/10.1186/s12977-018-0453-y

Meffre, E., A. Schaefer, H. Wardemann, P. Wilson, E. Davis, and M.C. Nussenzweig. 2004. Surrogate light chain expressing human peripheral B cells produce self-reactive antibodies. *J. Exp. Med.* 199:145–150. https://doi.org/10.1084/jem.20031550

Moreau, H.D., and P. Bousso. 2014. Disc. *Intravital*. 1:27–31. https://doi.org/10.4161/intv.21896

Mouquet, H. 2014. Antibody B cell responses in HIV-1 infection. *Trends Immunol.* 35:549–561. https://doi.org/10.1016/j.it.2014.08.007

Mouquet, H., F. Klein, J.F. Scheid, M. Warncke, J. Pietzsch, T.Y. Oliveira, K. Velinzon, M.S. Seaman, and M.C. Nussenzweig. 2011. Memory B cell antibodies to HIV-1 gp140 cloned from individuals infected with clade A and B viruses. *PLoS One*. 6:e24078. https://doi.org/10.1371/journal.pone.0024078

Mouquet, H., L. Scharf, Z. Euler, Y. Liu, C. Eden, J.F. Scheid, A. Halper-Stromberg, P.N. Gnanapragasam, D.I. Spencer, M.S. Seaman, et al. 2012. Complex-type N-glycan recognition by potent broadly neutralizing HIV antibodies. *Proc. Natl. Acad. Sci. USA*. 109:E3268–E3277. https://doi.org/10.1073/pnas.1217207109

Mouquet, H., J.F. Scheid, M.J. Zoller, M. Krogsgaard, R.G. Ott, S. Shukair, M.N. Artyomov, J. Pietzsch, M. Connors, F. Pereyra, et al. 2010. Polyreactivity increases the apparent affinity of anti-HIV antibodies by heteroligation. *Nature*. 467:591–595. https://doi.org/10.1038/nature09385

Moyo, T., D. Kitchin, and P.L. Moore. 2020. Targeting the N332-supersite of the HIV-1 envelope for vaccine design. *Expert Opin. Ther. Targets*. 24: 499–509. https://doi.org/10.1080/14728222.2020.1752183

Nabi, R., Z. Moldoveanu, Q. Wei, E.T. Golub, H.G. Durkin, R.M. Greenblatt, B.C. Herold, M.J. Nowicki, S. Kassaye, M.W. Cho, et al. 2017. Differences in serum IgA responses to HIV-1 gp41 in elite controllers compared to viral suppressors on highly active antiretroviral therapy. *PLoS One*. 12: e0180245. https://doi.org/10.1371/journal.pone.0180245

Nakane, T., D. Kimanius, E. Lindahl, and S.H. Scheres. 2018. Characterisation of molecular motions in cryo-EM single-particle data by multi-body refinement in RELION. *Elife*. 7:e36861. https://doi.org/10.7554/eLife.36861

Niessl, J., A.E. Baxter, P. Mendoza, M. Jankovic, Y.Z. Cohen, A.L. Butler, C.-L. Lu, M. Dubé, I. Shimeliovich, H. Gruell, et al. 2020. Combination anti-HIV-1 antibody therapy is associated with increased virus-specific T cell immunity. *Nat. Med.* 26:222–227. https://doi.org/10.1038/s41591-019-0747-1

Nishimura, Y., and M.A. Martin. 2017. Of mice, macaques, and men: broadly neutralizing antibody immunotherapy for HIV-1. *Cell Host Microbe*. 22: 207–216. https://doi.org/10.1016/j.chom.2017.07.010

Pettersen, E.F., T.D. Goddard, C.C. Huang, G.S. Couch, D.M. Greenblatt, E.C. Meng, and T.E. Ferrin. 2004. UCSF Chimera--a visualization system for exploratory research and analysis. *J. Comput. Chem.* 25:1605–1612. https://doi.org/10.1002/jcc.20084

Planchais, C., A. Kok, A. Kanyavuz, V. Lorin, T. Bruel, F. Guivel-Benhassine, T. Rollenske, J. Prigent, T. Hieu, T. Prazuck, et al. 2019. HIV-1 envelope recognition by polyreactive and cross-reactive intestinal B cells. *Cell Rep.* 27:572–585.e7. https://doi.org/10.1016/j.celrep.2019.03.032

Planque, S., M. Salas, Y. Mitsuda, M. Sienczyk, M.A. Escobar, J.P. Mooney, M.K. Morris, Y. Nishiyama, D. Ghosh, A. Kumar, et al. 2010. Neutralization of genetically diverse HIV-1 strains by IgA antibodies to the gp120-CD4-binding site from long-term survivors of HIV infection. *AIDS*. 24:875–884. https://doi.org/10.1097/QAD.0b013e3283376e88

Prabakaran, P., and P.S. Chowdhury. 2020. Landscape of non-canonical cysteines in human VH repertoire revealed by immunogenetic analysis. *Cell Rep.* 31:107831. https://doi.org/10.1016/j.celrep.2020.107831

Prigent, J., A. Jarossay, C. Planchais, C. Eden, J. Dufloo, A. Kok, V. Lorin, O. Vratskikh, T. Couderc, T. Bruel, et al. 2018. Conformational plasticity in broadly neutralizing HIV-1 antibodies triggers polyreactivity. *Cell Rep.* 23:2568–2581. https://doi.org/10.1016/j.celrep.2018.04.101

Prigent, J., V. Lorin, A. Kok, T. Hieu, S. Bourgeau, and H. Mouquet. 2016. Scarcity of autoreactive human blood IgA(+) memory B cells. *Eur. J. Immunol.* 46:2340–2351. https://doi.org/10.1002/eji.201646446

Pritchard, L.K., S. Vasiljevic, G. Ozorowski, G.E. Seabright, A. Cupo, R. Ringe, H.J. Kim, R.W. Sanders, K.J. Doores, D.R. Burton, et al. 2015. Structural constraints determine the glycosylation of HIV-1 envelope trimers. *Cell Rep.* 11:1604–1613. https://doi.org/10.1016/j.celrep.2015.05.017

Punjani, A., J.L. Rubinstein, D.J. Fleet, and M.A. Brubaker. 2017. cryoSPARC: algorithms for rapid unsupervised cryo-EM structure determination. *Nat. Methods*. 14:290–296. https://doi.org/10.1038/nmeth.4169

Punjani, A., H. Zhang, and D.J. Fleet. 2020. Non-uniform refinement: adaptive regularization improves single-particle cryo-EM reconstruction. *Nat. Methods*. 17:1214–1221. https://doi.org/10.1038/s41592-020-00990-8

Rohou, A., and N. Grigorieff. 2015. CTFFIND4: Fast and accurate defocus estimation from electron micrographs. *J. Struct. Biol.* 192:216–221. https://doi.org/10.1016/j.jsb.2015.08.008

Ruiz, M.J., Y. Ghiglione, J. Falivene, N. Laufer, M.P. Holgado, M.E. Socias, P. Cahn, O. Sued, L. Giavedoni, H. Salomon, et al. 2016. Env-specific IgA from viremic HIV-infected subjects compromises antibody-dependent cellular cytotoxicity. *J. Virol.* 90:670–681. https://doi.org/10.1128/JVI.02363-15

Santra, S., G.D. Tomaras, R. Warrier, N.I. Nicely, H.X. Liao, J. Pollara, P. Liu, S.M. Alam, R. Zhang, S.L. Cocklin, et al. 2015. Human non-neutralizing HIV-1 envelope monoclonal antibodies limit the number of founder viruses during SHIV mucosal infection in rhesus macaques. *PLoS Pathog.* 11:e1005042. https://doi.org/10.1371/journal.ppat.1005042

Sarzotti-Kelsoe, M., X. Daniell, C.A. Todd, M. Bilska, A. Martelli, C. LaBranche, L.G. Perez, C. Ochsenbauer, J.C. Kappes, W. Rountree, et al. 2014. Optimization and validation of a neutralizing antibody assay for HIV-1 in A3R5 cells. *J. Immunol. Methods*. 409:147–160. https://doi.org/10.1016/j.jim.2014.02.013

Scheepers, C., V. Bekker, C. Anthony, S.I. Richardson, B. Oosthuysen, T. Moyo, P. Kgagudi, D. Kitchin, M. Nonyane, T. York, et al. 2020. Antibody isotype switching as a mechanism to counter HIV neutralization escape. *Cell Rep.* 33:108430. https://doi.org/10.1016/j.celrep.2020.108430

Scheid, J.F., H. Mouquet, B. Ueberheide, R. Diskin, F. Klein, T.Y.K. Oliveira, J. Pietzsch, D. Fenyo, A. Abadir, K. Velinzon, et al. 2011. Sequence and structural convergence of broad and potent HIV antibodies that mimic CD4 binding. *Science*. 333:1633–1637. https://doi.org/10.1126/science.1207227

Schommers, P., H. Gruell, M.E. Abernathy, M.-K. Tran, A.S. Dingens, H.B. Gristick, C.O. Barnes, T. Schoofs, M. Schlotz, K. Vanshylla, et al. 2020. Restriction of HIV-1 escape by a highly broad and potent neutralizing antibody. *Cell*. 180:471–489.e22. https://doi.org/10.1016/j.cell.2020.01.010

Schoofs, T., C.O. Barnes, N. Suh-Toma, J. Golijanin, P. Schommers, H. Gruell, A.P. West Jr., F. Bach, Y.E. Lee, L. Nogueira, et al. 2019. Broad and potent neutralizing antibodies recognize the silent face of the HIV envelope. *Immunity*. 50:1513–1529.e9. https://doi.org/10.1016/j.immuni.2019.04.014

Seabright, G.E., C.A. Cottrell, M.J. van Gils, A. D'Addabbo, D.J. Harvey, A.-J. Behrens, J.D. Allen, Y. Watanabe, N. Scaringi, T.M. Polveroni, et al. 2020. Networks of HIV-1 envelope glycans maintain antibody epitopes in the face of glycan additions and deletions. *Structure*. 28:897–909.e6. https://doi.org/10.1016/j.str.2020.04.022

Seaton, K.E., A. Deal, X. Han, S.S. Li, A. Clayton, J. Heptinstall, A. Duerr, M.A. Allen, X. Shen, S. Sawant, et al. 2021. Meta-analysis of HIV-1 vaccine elicited mucosal antibodies in humans. *NPJ Vaccin.* 6:56. https://doi.org/10.1038/s41541-021-00305-8

Simonich, C.A., K.L. Williams, H.P. Verkerke, J.A. Williams, R. Nduati, K.K. Lee, and J. Overbaugh. 2016. HIV-1 neutralizing antibodies with limited hypermutation from an infant. *Cell*. 166:77–87. https://doi.org/10.1016/j.cell.2016.05.055

Sok, D., M. Pauthner, B. Briney, J.H. Lee, K.L. Saye-Francisco, J. Hsueh, A. Ramos, K.M. Le, M. Jones, J.G. Jardine, et al. 2016. A prominent site of antibody vulnerability on HIV envelope incorporates a motif associated with CCR5 binding and its camouflaging glycans. *Immunity*. 45:31–45. https://doi.org/10.1016/j.immuni.2016.06.026

Sok, D., M.J. van Gils, M. Pauthner, J.P. Julien, K.L. Saye-Francisco, J. Hsueh, B. Briney, J.H. Lee, K.M. Le, P.S. Lee, et al. 2014. Recombinant HIV envelope trimer selects for quaternary-dependent antibodies targeting the trimer apex. *Proc. Natl. Acad. Sci. USA*. 111:17624–17629. https://doi.org/10.1073/pnas.1415789111

Steffen, U., C.A. Koeleman, M.V. Sokolova, H. Bang, A. Kleyer, J. Rech, H. Unterweger, M. Schicht, F. Garreis, J. Hahn, et al. 2020. IgA subclasses have different effector functions associated with distinct glycosylation profiles. *Nat. Commun.* 11:120. https://doi.org/10.1038/s41467-019-13992-8

Stephenson, K.E., K. Wagh, B. Korber, and D.H. Barouch. 2020. Vaccines and broadly neutralizing antibodies for HIV-1 prevention. *Annu. Rev.*

Immunol. 38:673–703. https://doi.org/10.1146/annurev-immunol-080219-023629

Tay, M.Z., P. Liu, L.D. Williams, M.D. McRaven, S. Sawant, T.C. Gurley, T.T. Xu, S.M. Dennison, H.X. Liao, A.L. Chenine, et al. 2016. Antibody-mediated internalization of infectious HIV-1 virions differs among antibody isotypes and subclasses. *PLoS Pathog.* 12:e1005817. https://doi.org/10.1371/journal.ppat.1005817

Tiller, T., E. Meffre, S. Yurasov, M. Tsuiji, M.C. Nussenzweig, and H. Wardemann. 2008. Efficient generation of monoclonal antibodies from single human B cells by single cell RT-PCR and expression vector cloning. *J. Immunol.Methods.* 329:112–124. https://doi.org/10.1016/j.jim.2007.09.017

Tomaras, G.D., G. Ferrari, X. Shen, S.M. Alam, H.X. Liao, J. Pollara, M. Bonsignori, M.A. Moody, Y. Fong, X. Chen, et al. 2013. Vaccine-induced plasma IgA specific for the C1 region of the HIV-1 envelope blocks binding and effector function of IgG. *Proc. Natl. Acad. Sci. USA.* 110:9019–9024. https://doi.org/10.1073/pnas.1301456110

Trama, A.M., M.A. Moody, S.M. Alam, F.H. Jaeger, B. Lockwood, R. Parks, K.E. Lloyd, C. Stolarchuk, R. Scearce, A. Foulger, et al. 2014. HIV-1 envelope gp41 antibodies can originate from terminal ileum B cells that share cross-reactivity with commensal bacteria. *Cell Host Microbe.* 16:215–226. https://doi.org/10.1016/j.chom.2014.07.003

Trkola, A., M. Purtscher, T. Muster, C. Ballaun, A. Buchacher, N. Sullivan, K. Srinivasan, J. Sodroski, J.P. Moore, and H. Katinger. 1996. Human monoclonal antibody 2G12 defines a distinctive neutralization epitope on the gp120 glycoprotein of human immunodeficiency virus type 1. *J. Virol.* 70:1100–1108. https://doi.org/10.1128/JVI.70.2.1100-1108.1996

van Royen-Kerkhof, A., E.A. Sanders, V. Walraven, M. Voorhorst-Ogink, E. Saeland, J.L. Teeling, A. Gerritsen, M.A. van Dijk, W. Kuis, G.T. Rijkers, et al. 2005. A novel human CD32 mAb blocks experimental immune haemolytic anaemia in FcgammaRIIA transgenic mice. *Br. J. Haematol.* 130:130–137. https://doi.org/10.1111/j.1365-2141.2005.05571.x

Victora, G.D., and H. Mouquet. 2018. What are the primary limitations in B cell affinity maturation, and how much affinity maturation can we drive with vaccination? Lessons from the antibody response to HIV-1. *Cold Spring Harb. Perspect. Biol.* 10:a029389. https://doi.org/10.1101/cshperspect.a029389

Walker, L.M., M. Huber, K.J. Doores, E. Falkowska, R. Pejchal, J.P. Julien, S.K. Wang, A. Ramos, P.Y. Chan-Hui, M. Moyle, et al. 2011. Broad neutralization coverage of HIV by multiple highly potent antibodies. *Nature.* 477:466–470. https://doi.org/10.1038/nature10373

Wardemann, H., and J. Kofer. 2013. Expression cloning of human B cell immunoglobulins. *Methods Mol. Biol.* 971:93–111. https://doi.org/10.1007/978-1-62703-269-8_5

Wardemann, H., S. Yurasov, A. Schaefer, J.W. Young, E. Meffre, and M.C. Nussenzweig. 2003. Predominant autoantibody production by early human B cell precursors. *Science.* 301:1374–1377. https://doi.org/10.1126/science.1086907

Williams, C.J., J.J. Headd, N.W. Moriarty, M.G. Prisant, L.L. Videau, L.N. Deis, V. Verma, D.A. Keedy, B.J. Hintze, V.B. Chen, et al. 2018. MolProbity: More and better reference data for improved all-atom structure validation. *Protein Sci.* 27:293–315. https://doi.org/10.1002/pro.3330

Williams, W.B., H.X. Liao, M.A. Moody, T.B. Kepler, S.M. Alam, F. Gao, K. Wiehe, A.M. Trama, K. Jones, R. Zhang, et al. 2015. HIV-1 VACCINES. Diversion of HIV-1 vaccine-induced immunity by gp41-microbiota cross-reactive antibodies. *Science.* 349:aab1253. https://doi.org/10.1126/science.aab1253

Wills, S., K.K. Hwang, P. Liu, S.M. Dennison, M.Z. Tay, X. Shen, J. Pollara, J.T. Lucas, R. Parks, S. Rerks-Ngarm, et al. 2018. HIV-1-Specific IgA monoclonal antibodies from an HIV-1 vaccinee mediate galactosylceramide blocking and phagocytosis. *J. Virol.* 92:e01552-17. https://doi.org/10.1128/JVI.01552-17

Woof, J.M., and J. Mestecky. 2015. Chapter 17 - mucosal immunoglobulins. *In* Mucosal Immunology. J. Mestecky, W. Strober, M.W. Russell, B.L. Kelsall, H. Cheroutre, and B.N. Lambrecht, editors. Fourth Edition. Academic Press, Boston. 287–324

Wu, X., Z. Zhang, C.A. Schramm, M.G. Joyce, Y.D. Kwon, T. Zhou, Z. Sheng, B. Zhang, S. O'Dell, K. McKee, et al. 2015. Maturation and diversity of the VRC01-antibody lineage over 15 Years of chronic HIV-1 infection. *Cell.* 161:470–485. https://doi.org/10.1016/j.cell.2015.03.004

Yang, X., M. Farzan, R. Wyatt, and J. Sodroski. 2000. Characterization of stable, soluble trimers containing complete ectodomains of human immunodeficiency virus type 1 envelope glycoproteins. *J. Virol.* 74:5716–5725. https://doi.org/10.1128/jvi.74.12.5716-5725.2000

Zhang, J., K. Kobert, T. Flouri, and A. Stamatakis. 2013. PEAR: a fast and accurate Illumina paired-end reAd mergeR. *Bioinformatics.* 30:614–620. https://doi.org/10.1093/bioinformatics/btt593

Zheng, S.Q., E. Palovcak, J.P. Armache, K.A. Verba, Y. Cheng, and D.A. Agard. 2017. MotionCor2: anisotropic correction of beam-induced motion for improved cryo-electron microscopy. *Nat. Methods.* 14:331–332. https://doi.org/10.1038/nmeth.4193

JEM

Supplemental material

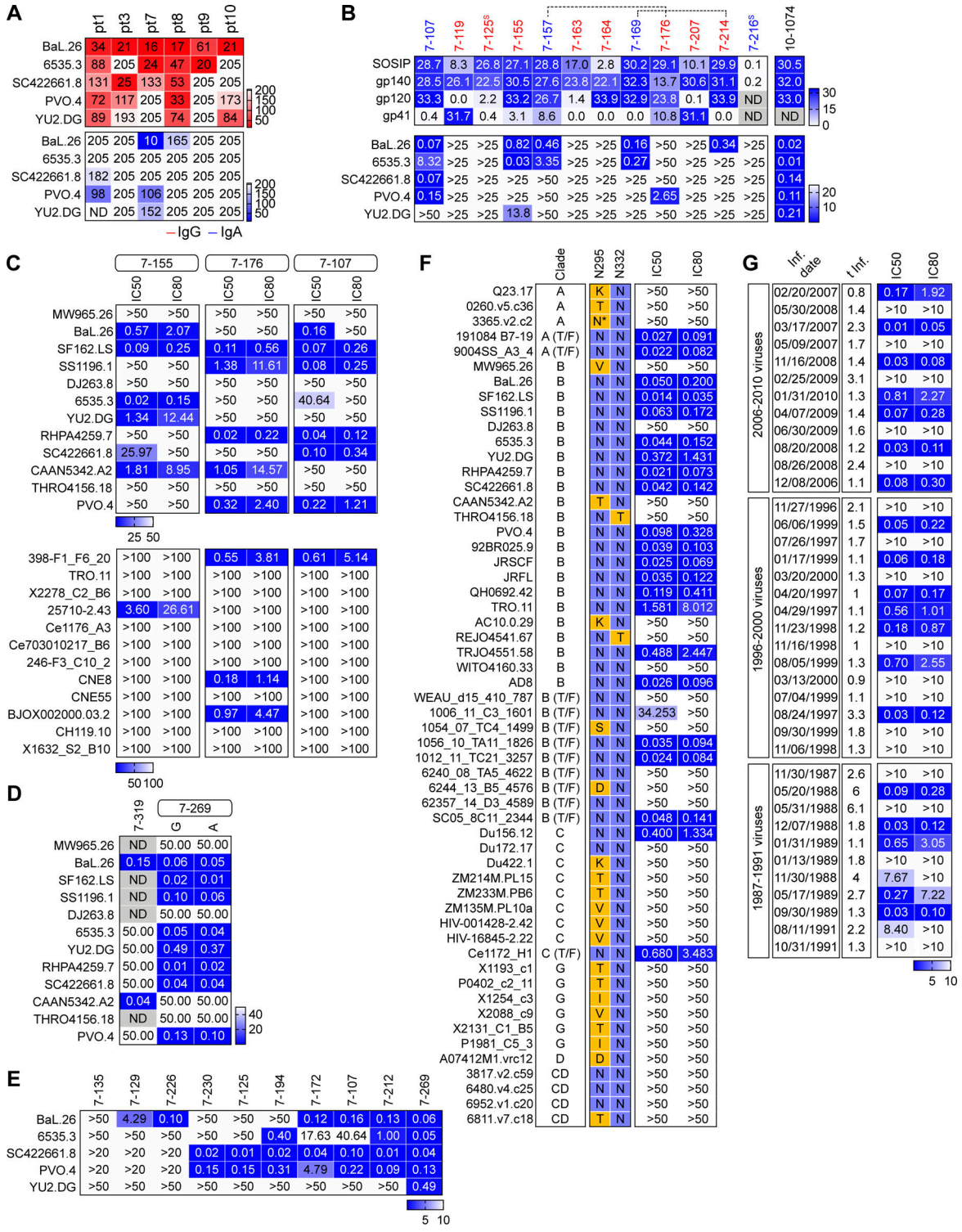

Figure S1. **HIV-1 neutralization by pt7 serum and monoclonal antibodies. (A)** Table shows the neutralizing activity of serum IgGs and IgAs purified from six viremic controllers against selected clade B viruses (n = 5). IC_{50} values (µg/ml) are indicated in cell center. Darker colors indicate higher potency; white, no neutralization. **(B)** Tables comparing ELISA binding to HIV-1 Env proteins (top) and neutralizing activity against selected clade B viruses (n = 5, bottom) of monoclonal antibodies cloned from pt7 blood IgG^+ (red) and IgA^+ (blue) memory B cells. 7-125^S and 7-216^S, SOSIP-isolated antibodies. Darker colors indicate higher Env reactivity or neutralization potency; white, no binding or neutralization. ELISA AUC and IC_{50} values (µg/ml) are indicated in cell center. Dotted links indicate clonally related members. 10-1074 is the positive control. **(C)** Table shows the neutralizing activity of selected antibodies produced as recombinant IgGs against 12-virus reference panels. IC_{50} and IC_{80} values (µg/ml) are indicated in cell center. Darker colors indicate higher potency; white, no neutralization. **(D)** Same as C but for clade B viruses only and 7-319 IgG, 7-269 IgG and IgA antibodies. IC_{50} values (µg/ml) are shown. **(E)** Same as B but for 7-107 clonal variants expressed as IgGs. **(F)** Same as C but for 7-269 IgA against a cross-clade extended panel (n = 56). For each viral strain, amino acids at PNGS N295 and N332 are indicated. **(G)** Same as F but with clade B viruses from three epidemic periods.

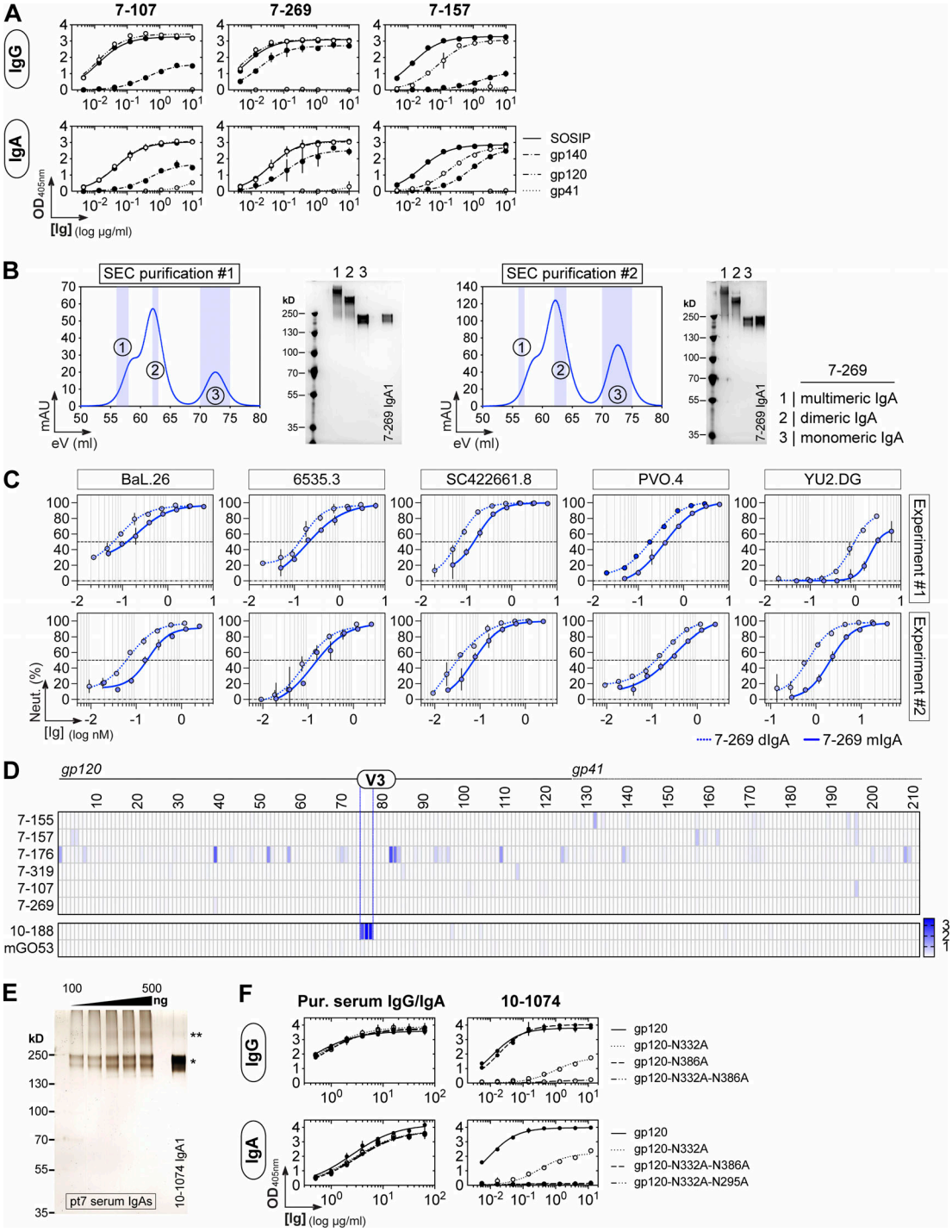

Figure S2. **IgA profiles of pt7 bNAbs and purified serum antibodies. (A)** ELISA binding analysis comparing the reactivity of pt7 bNAbs expressed as IgG and IgA against HIV-1 Env proteins. Means ± SD of duplicate OD values are shown. **(B)** Purification of monomeric and dimeric 7-269 IgA antibodies. FPLC chromatograms show the protein separation of IgA monomers, dimers, and multimers by SEC in two separate experiments. The x axis shows the elution volume (eV) required to obtain the values of absorption units at 280 nm (mAU) indicated on the y axis. Light blue bars indicate selected fractions. Silver-stained SDS-PAGE gels on the right show the protein bands in the purified pooled fractions. **(C)** Graphs comparing the neutralizing activity of monomeric and dimeric 7-269 IgA antibodies (mIgA and dIgA, respectively) against the selected pseudoviruses as measured in the in vitro TZM-bl assay. Means ± SD of duplicate values for two independent experiments are shown. mIgA and dIgA antibodies from purification 1 were tested in neutralization experiment 1, and mIgA and dIgA antibodies from purification 2 were used in experiment 2. **(D)** Heatmap showing the ELISA binding analysis of selected pt7 bNAbs against consensus subtype B overlapping Env peptides. Darker colors indicate higher reactivity (OD values); white, no binding. Non–HIV-1 mGO53 and anti-V3^{crown} 10-188 antibody are negative and positive controls, respectively. **(E)** Silver-stained SDS-PAGE gel shows purified pt7 serum IgAs (ranging from 100 to 500 ng) in nonreducing and nonheated conditions. Monomeric 10-1074 IgA1 antibodies were used as a control. * and ** indicate monomeric and dimeric IgA antibodies, respectively. **(F)** ELISA binding analysis comparing the reactivity of purified IgG and IgA antibodies from pt7 serum against HIV-1 Env gp120 and selected mutant proteins. Means ± SD of triplicate OD values are shown. 10-1074 IgG1 and IgA1 antibodies were used as controls.

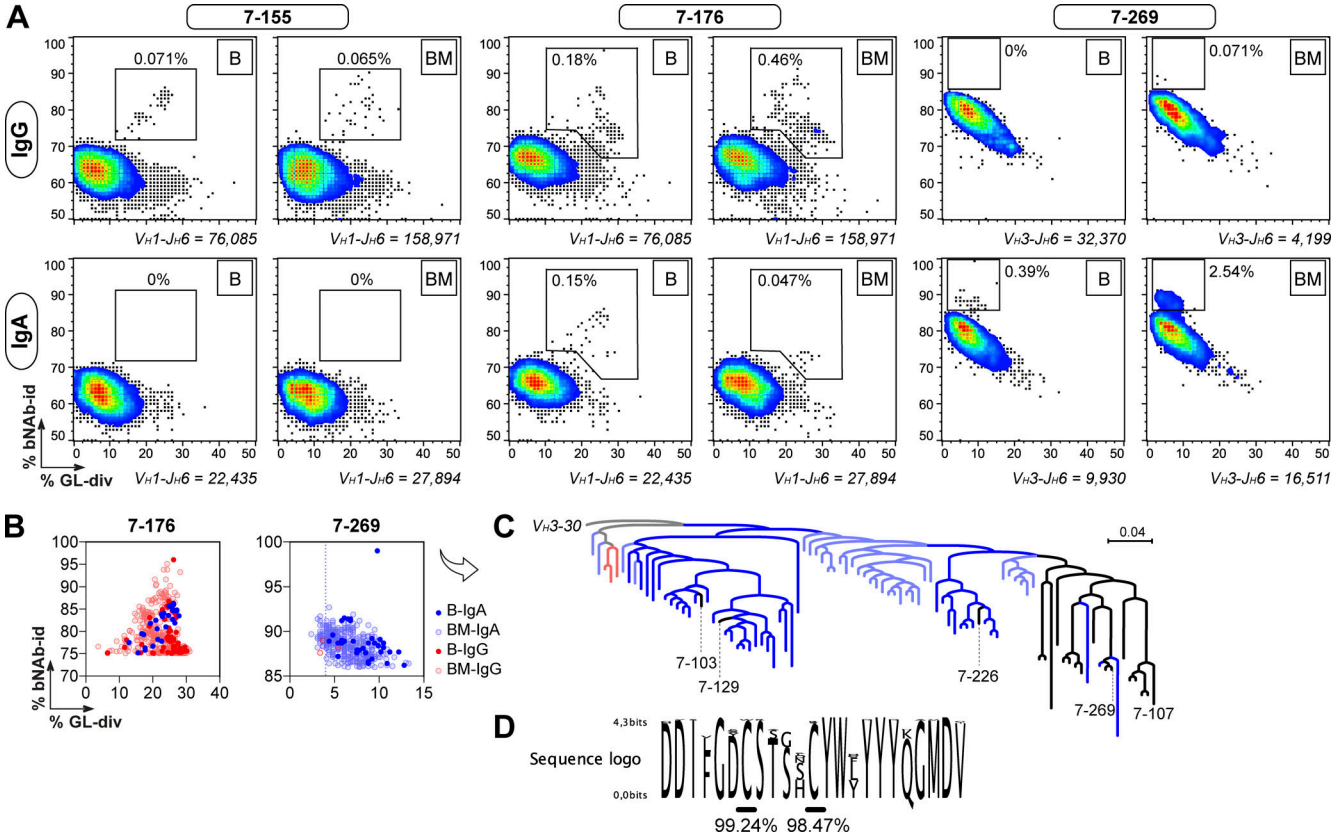

Figure S3. **Lineage tracing of pt7 bNAbs in the blood and bone marrow. (A)** Plots show divergence/identity analysis of pt7 IgG and IgA heavy chain (IgH) sequences obtained by Ig-HTS from peripheral blood (B) and bone marrow (BM) mononuclear cells. IgH sequences filtered on bNAb-specific V-J rearrangements (total numbers are shown below the plots) are depicted as function of the identity to bNAb reference sequence (% bNAb-id) and of divergence to inferred GL sequence (% GL-div). Gate numbers indicate the % of bNAb-relative sequences. **(B)** Divergence/identity plots showing the overlay of 7-176 and 7-269 sequences from pt7 blood and bone marrow IgA and IgG DNA libraries as shown in A. **(C)** Phylogenic tree (right) shows the relationship between 7-269 clonally related IgH nucleotide sequences found by high-throughput sequencing in blood and bone marrow IgA-expressing cells (in dark and light blue, respectively) and the bone marrow IgG repertoire (in light red) as shown in B, and by single B cell gp160-capture (as shown in Fig. 1 D, blue) used as reference sequences (in black). Only bone marrow 7-269–related sequences with GL divergence ≤4% were included in the phylogenic analysis. **(D)** Sequence logo showing the alignment of the CDR_H3s from the V_H sequences obtained by Ig-HTS shown in C (n = 131). The frequency of Cys residues in position 105 and 110 is shown below.

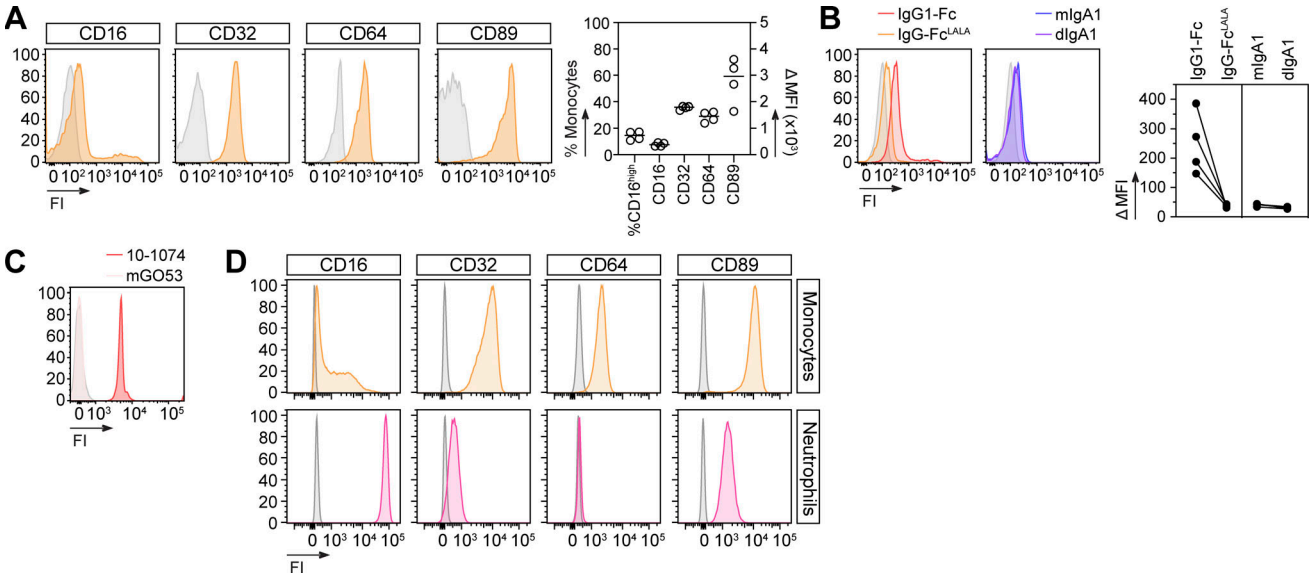

Figure S4. **Fc receptor expression on human immune effector cells. (A)** Representative flow cytometric histogram showing the surface expression of selected Fc receptors (FcR) on purified human monocytes used for ADCP with gp140-coupled beads (left). FI, fluorescence intensity. Gray histograms correspond to unstained cell controls. Dot plot shows the surface expression of selected FcR on human monocytes purified from four donors (right). Percentage of $CD16^{high}$ cells (left y axis) and ΔMFI for all FcR are shown. **(B)** Representative flow cytometric histogram showing the binding of recombinant Fc proteins and IgA1 antibodies to purified human monocytes used for ADCP with gp140-coupled beads (left). Dot plot shows the binding of Fc proteins and IgA1 antibodies to human monocytes purified from four donors (right). m, monomeric; d, dimeric. **(C)** Representative flow cytometric histogram showing the binding of 10-1074 IgG antibodies to YU2 gp140-F-coupled FITC beads. mGO53 antibody is the negative isotypic control. **(D)** Same as in A but for purified human monocytes and neutrophils used as effectors in co-culture with HIV-1–infected CEM-NKR-CCR5 cells.

A

Glycan	Sugar residue in gp120 (chain B)	Residue in IgH (O) or IgL (P)	Distance (Å)
N295-glycan	B: NAG648 (O6)	O: S108 (O)	2.22
	B: NAG648 (O7)	O: Y115 (OH)	2.32
	B: NAG649 (N2)	O: T107 (O)	3.30
	B: MAN653 (O3)	O: Y59 (OH)	3.13
	B: MAN653 (O6)	O: W112 (NE1)	3.37
	B: MAN650 (O2)	O: Y111 (OH)	2.47
N332-glycan	B: MAN682 (O6)	P: T57 (OG1)	3.11
	B: MAN682 (O2)	P: R45 (NE)	3.48
	B: MAN682 (O3)	P: V46 (N)	2.92
	B: MAN682 (O5)	P: T57 (OG1)	3.23
	B: MAN659 (O3)	O: K98 (NZ)	2.88
N262-glycan	B: MAN686 (O2)	O: R31 (NH1)	2.29
	B: MAN686 (O3)	O: R31 (NE)	2.88
	B: MAN686 (O3)	O: R31 (NH1)	2.95

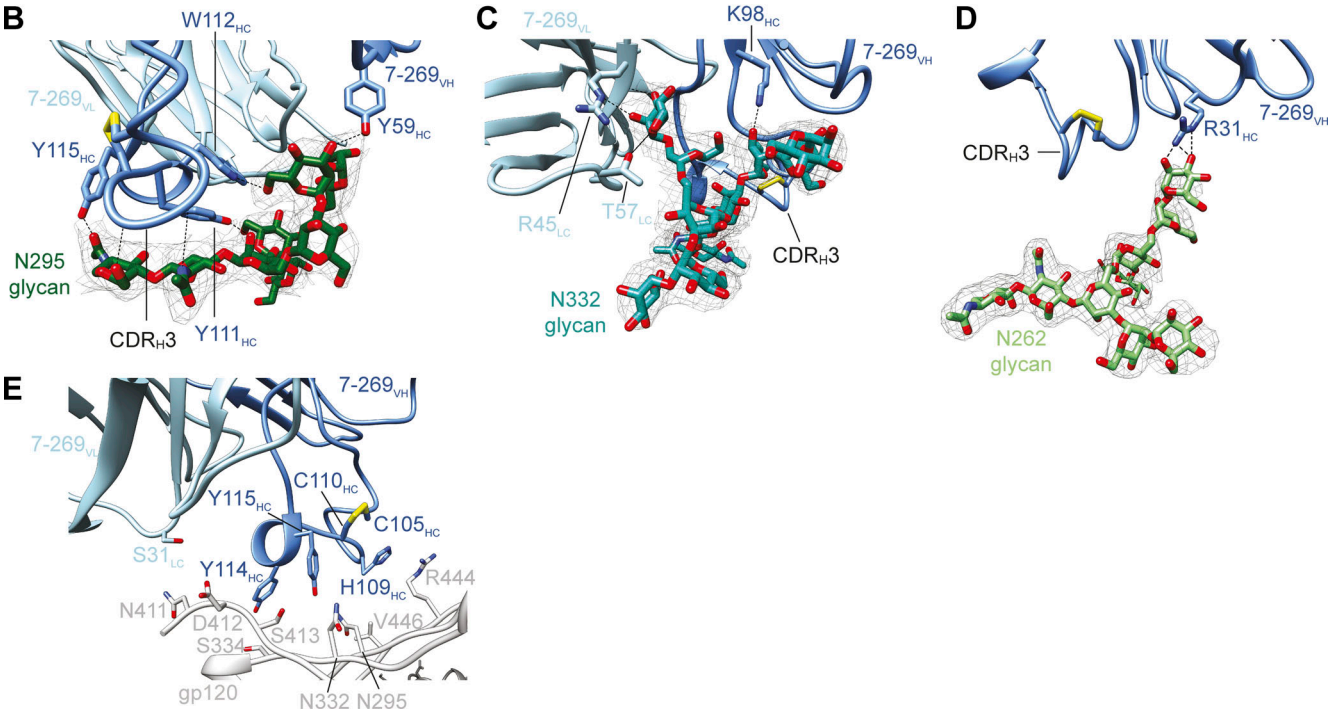

Figure S5. **Interactions at the BG505 SOSIP-7-269 Fab interface. (A–D)** Potential hydrogen bonds formed at the interface of the BG505 SOSIP-7-269 IgA Fab complex. The table in A indicates the atoms involved in forming potential hydrogen bonds at the complex interface and the distance between them. This information is also represented in B–D, where the electron density in which the glycans were built is also shown. **(E)** Stick representation of residues forming Van der Waals contacts between 7-269 and the gp120 protein subunit. The disulfide bond between C105 and C110 in the CDR_H3 is also represented as sticks. For better clarity, glycans are not shown.

Table S1, Table S2, Table S3, Table S4, Table S5, Data S1, and Data S2 are provided online. Table S1 lists immunoglobulin gene repertoire and reactivity of Env-captured human memory B cell antibodies from pt7. Table S2 lists human proteoarray hits for 7-176 antibody cross-reactivity to human proteins. Table S3 lists cryo-EM data collection, refinement, and validation statistics for BG505 SOSIP-7-269 Fab complexes. Table S4 lists buried surface area of 7-269 for each gp120 glycan. Table S5 lists buried surface area of gp120 for 7-269 Fab IgH and IgL. Data S1 provides cryo-EM data collection and processing of the SOSIP-7-269-3BNC117 complex. A micrograph with particles, selected 2D class averages, a local resolution graphic, and a scheme with the steps followed to process the collected data (along with GSFSC resolution plots) are shown for the SOSIP-7-269-3BNC117 complex. Data S2 provides cryo-EM data collection and processing of the SOSIP-7-155 and SOSIP-7-176 complexes. A micrograph with particles, selected 2D class averages, a local resolution graphic, and a scheme with the steps followed to process the collected data (along with GSFSC resolution plots) are shown for the SOSIP-7-155 (A) and SOSIP-7-176 (B) complexes.